INSTITUT NATIONAL DE RECHERCHE EN INFORMATIQUE ET EN AUTOMATIQUE

Physically Based Rigid Registration of 3-D Free-Form Objects: Application to Medical Imaging

Grégoire Malandain , Sara Fernández-Vidal

et Jean-Marie Rocchisani

N° 2453

Janvier 1995

PROGRAMME 4

ISSN 0249-6399

INRIA
SOPHIA ANTIPOLIS

Physically Based Rigid Registration of 3-D Free-Form Objects: Application to Medical Imaging

Grégoire Malandain *, Sara Fernández-Vidal
et Jean-Marie Rocchisani **

Programme 4 — Robotique, image et vision
Projet Epidaure

Rapport de recherche n° 2453 — Janvier 1995 — 60 pages

Abstract: The registration of 3-D objects is an important problem in computer vision and especially in medical imaging. It arises when data acquired by different sensors and/or at different times have to be fused. Under the basic assumption that the objects to be registered are rigid, the problem is to recover the six parameters of a rigid transformation. If landmarks or common characteristics are not available, the problem has to be solved by an iterative method. However such methods are inevitably attracted to local minima.

This paper presents a novel iterative method designed for the rigid registration of 3-D objects. Its originality lies in its physical basis: instead of minimizing an energy function with respect to the parameters of the rigid transformation (the classical approach) the minimization is achieved by studying the motion of a rigid object in a potential field. In particular, we consider the kinetic energy of the solid during the registration process, which allows it to "jump over" some local maxima of the potential energy and so avoid some local minima of that energy.

We present extensive experimental results on real 3-D medical images. In this particular application, we perform the matching process with the whole segmented volumes.

Key-words: 3D medical images, dynamics, matching, minimization of potential energy

(Résumé : tsvp)

*greg@sophia.inria.fr - INRIA, Project Epidaure - 2004 Route des Lucioles, BP 93 - 06902 Sophia Antipolis Cedex, France

**rocchi@bora.inria.fr - Hôpital Avicenne - Service de Médecine Nucléaire - 125 rue de Stalingrad - 93000 Bobigny, France

Unité de recherche INRIA Sophia-Antipolis
2004 route des Lucioles, BP 93, 06902 SOPHIA-ANTIPOLIS Cedex (France)
Téléphone : (33) 93 65 77 77 – Télécopie : (33) 93 65 77 65

Mise en correspondance d'objets 3D par une méthode physique : application à l'imagerie médicale

Résumé : La mise en correspondance des objets tridimensionnels est un problème important en vision par ordinateur, et particulièrement en imagerie médicale. Il apparaît lorsque des données acquises par des capteurs différents et/ou à des instants différents doivent être combinées. Avec la seule hypothèse que les objets à mettre en correspondance sont rigides, le problème se ramène à trouver les six paramètres d'une transformation rigide. Si des amers ou des caractéristiques communes ne sont pas présents, ce problème peut alors être résolu par une méthode itérative. Cependant, ces méthodes sont très sensibles aux minima locaux.

Cet article présente une nouvelle méthode itérative pour la mise en correspondance rigide d'objets tridimensionnels. Son originalité réside dans ses fondements physiques : au lieu de minimiser une fonction d'énergie par rapport aux paramètres de la transformation rigide (l'approche classique), la minimisation se fait en étudiant le mouvement d'un solide dans un champ de potentiel. En particulier, nous considérons l'énergie cinétique du solide durant le processus de minimisation, ce qui lui permet de "franchir" des barrières d'énergie potentiel et d'éviter ainsi des minima locaux de cette énergie.

Nous présentons des résultats expérimentaux sur des exemples médicaux réels. Dans cette application particulière, nous utilisons les objets volumiques segmentés et non leurs surfaces.

Mots-clé : imagerie médicale, image volumique, fusion de données, mécanique des solides, mise en correspondance d'images, minimisation d'énergie potentielle

1 Introduction

Registration is an important problem in computer vision. It comprises several different kinds of problem (see Brown [9] for a broad overview of registration techniques):

- registration of images of the same scene acquired from different sensors;
- registration of images of the same scene taken from different viewpoints;
- registration of images of the same scene taken at different times;
- location of an object in an image, or object recognition [63].

An important application area of registration techniques is in medical imaging. Because of significant improvements in medical imaging devices, three dimensional (3-D) images play an increasingly important role. Different imaging modalities provide the physician with complementary information: anatomy is usually obtained by X-ray Computed Tomography (CT), Magnetic Resonance Imaging (MRI) or ultrasound, whereas functional information is provided by Single Photon Emission Computed Tomography (SPECT), Positron Emitting Tomography (PET), or, to a limited extend, MRI.

In many cases it would be useful to combine several studies of the same patient. These include: to track and to quantify the evolution of a pathology, to evaluate a therapy, to locate the site of a metabolism (see figure 18 where anatomical information is superimposed on functional one), or to label the anatomical structures from an atlas.

Because these applications require extremely accurate quantitative results and because of the large volumes of data to be processed, an automatic method of registration is necessary. Moreover, this registration has to be performed in 3-D, for two reasons. First, the protocols for image acquisition vary from one image modality to another. Second, even between two images of the same modality, the position of the patient with respect to the acquisition device is seldom known perfectly.

There exists a wide variety of registration methods for medical applications in the literature (see van den Elsen et al. for a recent survey [70]). Several voxel intensity based methods have been proposed to maximize a similarity index [46, 71], to minimize the variance of image ratio [72], or to maximize a cross-correlation function [57]. The first two techniques give good results for PET or SPECT images but have not designed for other images. The third one has only been applied to 2-D images, and is not adapted to 3-D ones. As voxel intensity is obviously not invariant between images of different modalities, image segmentation is first necessary in order to obtain landmarks.

Markers have been widely used: external points on a stereotaxic frame or customized head holder which can be viewed in several modalities [17, 45, 49, 68, 73, 76], or internal landmarks (distinguished anatomical points, such as blood vessel bifurcations [31]). The transformation parameters are then computed by a conventional method (for instance, least squares method). However, external markers force the patient to carry a stereotaxic frame between successive acquisitions. Moreover, registration with previously recorded images is not possible. Internal landmarks often require manual detection, whose accuracy depends on image resolution, and which has a large effect on the computation of the transformation parameters. A local matching technique, based on crest lines, is described in [65, 66, 69]. It is feature-based, relatively robust to noise, resolution and anatomical variations; but it works only for good quality and high resolution images.

Instead of segmenting only a few features points as in the methods presented above, our approach is more global and uses considerably more information, such as a complete organ (like the brain). A preliminary segmentation method must yield two sets of points such that a significant subset of the first can be rigidly superimposed on a subset of the second[1]. Since this segmentation may be imperfect, or objects to be registered may be somewhat different, we seek a 3-D rigid registration method that performs well in the presence of occlusions. Moreover, for the same reasons, a transformation between the two data sets cannot be sought globally, for example by superposing the centers of inertia, and aligning the axes of inertia [1, 59].

Many registration techniques that tolerate occlusions can be found in the literature of computer vision and robotics [2, 6, 27] and also in the medical field [29, 37, 44]. These include: prediction-verification, geometric hashing or Hough techniques as described in [2, 27, 29]. However, because of the large number of points involved in a segmentation of a 3-D image, such techniques are much too costly, since their computational complexity grows quadratically with the number of model points. On the other hand, iterative methods based on potentials of attraction, such as those described in [6, 8, 12, 21, 28, 33, 37, 44, 51, 69, 74] are more able. Faber et al. [19] use a similar method for 3-D rigid registration, which is carried out before 1-D temporal registration in the 4-D registration of MRI and SPECT time series of the heart. Methods of this sort suffer from local minima. Techniques to overcome this problem include using several initial positions [6, 8] and/or a hierarchical approach [8, 50].

[1] We assume that such a minimal segmentation procedure can always be found. This preliminary condition is much less restrictive than demanding a perfect segmentation of at least one of the images. Such methods have already been presented for the brain in [10, 24, 34, 56, 75] and also for other organs in [11, 16]. In our results, 3-D mathematical morphology [61, 62] is sufficient to treat all presented examples in a completely automatic process.

In this paper, a novel iterative rigid registration method is proposed based on potential minimization. One of the images will generate a potential of attraction, creating a dynamic evolution of the second image towards an "optimal" registration position. The originality of the paper stems from the dynamic behavior of this system, which can be compared to the motion of a solid under the action of a potential field and which offers a intuitive understanding of the minimization process. Our approach considers the kinetic energy of the solid during the registration process, and this enables many local minima to be avoided. In practice, as our extensive experimental results show, local minima can be avoided and images of different modalities registered.

We apply our method to real medical images. Instead of using only the surface of the segmented objects for matching, we use the whole segmented volume. To keep a reasonable computational cost, we present some subsampling methods adapted to our approach.

This method, combined to a segmentation method, is about to be marketed by Focus-Medical (Grenoble, France) for medical applications.

2 Method

In this section, a general iterative method for the rigid registration of two free-form objects is proposed. We assume that the objects to be registered are already known (in our medical applications, we consider that objects are already segmented).

One of the objects, which will be called the reference object or solid in the following, and denoted by R, generates a potential field p: the rigid registration of the objects consists in finding the potential minimum for the second object, which we call the moving object or solid and denote by S.

A number of methods [6, 8, 12, 33, 37, 44, 51, 69, 74] already exist, which explicitly minimize a potential energy by deriving it with respect to the transformation parameters. Instead we use the Lagrange equations with respect to the transformation parameters, because they introduce dynamic in the registration process.

Using these equations, a conventional method to achieve the registration is:

1. to ensure the convergence, one may add an energy dissipation term;
2. one discretizes the equations in time, using explicit Euler methods;
3. to find a minimum, one solves these equations for new transformations parameters, using a some small time step, and iterates until the system stabilizes.

Our approach differs from the above one in two points:

1. instead of Euler methods, we propose to use a second order Taylor expansion to compute new values of transformations parameters, because it is more appropriate to "jump over" local minima;

2. instead of a continuous dissipation term, we decrease the energy by steps, so we do not have to tune any viscosity parameter.

2.1 Lagrange equations

Let the moving solid S have center of mass G, which we assume to be moving towards R with linear velocity $\mathbf{v}(G)$ and angular velocity $\boldsymbol{\omega}$. The inertia tensor of S, taken about G is denoted $\mathbf{J}(G)$. Similarly, we suppose that there is a potential $p(P)$ at each point P of S. Then, the kinetic energy E_K and the potential energy E_P of the moving solid S are given, as usual, by:

$$E_K = \frac{1}{2}\left(m(S)\,\mathbf{v}(G)^2 + \boldsymbol{\omega}.\mathbf{J}(G)\boldsymbol{\omega}\right) \quad (1)$$

$$E_P = \int_S p(P)dv(P) \ . \quad (2)$$

Defining the Lagrangian $L = E_K - E_P$, the Lagrange equations are:

$$\frac{\mathrm{d}}{\mathrm{d}t}\left(\frac{\partial L}{\partial \dot{q}_i}\right) - \frac{\partial L}{\partial q_i} = 0 \qquad i = 1 \ldots 6 \quad (3)$$

where q_i is one of the 6 parameters of the rigid transformation. Assuming as usual that the potential energy is independent of the derivatives of the transformation parameters, equation (3) may be written:

$$\frac{\mathrm{d}}{\mathrm{d}t}\left(\frac{\partial E_K}{\partial \dot{q}_i}\right) - \frac{\partial E_K}{\partial q_i} = -\frac{\partial E_P}{\partial q_i} \qquad i = 1 \ldots 6 \quad (4)$$

2.2 Transformation parameters

We define the position of the solid S during its motion by the rigid transformation between its initial position (at time $t = 0$) and its current position (at time t). The transformation is given by a rotation matrix $\mathbf{R}$ and a translation vector $\mathbf{t}$.

We denote the initial position of the center of mass of S by G_0 and the current one by $G(t)$. Similarly a point $P(t)$ of S is related to its initial position P_0 by:

$$\begin{cases} \mathbf{t} & = \overrightarrow{G_0G(t)} & \text{(5a)} \\ \overrightarrow{G(t)P(t)} & = \mathbf{R}\,\overrightarrow{G_0P_0} & \text{(5b)} \end{cases}$$

In the following, whenever it is clear, we will omit explicit mention of time t. Equations (5) are equivalent to:

$$\overrightarrow{OP} = \mathbf{R}\,\overrightarrow{G_0P_0} + \overrightarrow{OG_0} + \mathbf{t} \tag{6}$$

where O is the center of coordinates.

Because of the rotation matrix, the inertia tensor $\mathbf{J}$ of S at time t (see section A.1) can be expressed with respect to the initial inertia tensor $\mathbf{J}_0$ by:

$$\mathbf{J} = \mathbf{R}\,\mathbf{J}_0\,\mathbf{R}^T \tag{7}$$

For the reasons given in appendix B, we represent the rotation by a rotation vector $\mathbf{r}$, which is related to the usual rotation matrix by Rodrigues' formula (29).

Differentiating equation (5a), we relate the derivatives of the translation vector to both the velocity and the acceleration of G:

$$\dot{\mathbf{t}} = \mathbf{v}(G) \quad \text{and} \quad \ddot{\mathbf{t}} = \boldsymbol{\gamma}(G) \tag{8}$$

Differentiating equation (5b), we obtain:

$$\mathbf{v}(P) - \mathbf{v}(G) = \dot{\mathbf{R}}\,\overrightarrow{G_0P_0}$$

Substituting equation (5b) into the velocities composition rule (22) yields:

$$\mathbf{v}(P) = \mathbf{v}(G) + \boldsymbol{\omega} \wedge \mathbf{R}\,\overrightarrow{G_0P_0}$$

By combining these two last equations, we relate the derivative of the rotation matrix to itself and the angular velocity vector:

$$\dot{\mathbf{R}} = \mathbf{X}(\boldsymbol{\omega})\mathbf{R}$$

where $\mathbf{X}(\boldsymbol{\omega})$ is a matrix operator which corresponds to vector product by $\boldsymbol{\omega}$. Please notice that this notation of the vector product will be used below. Taking into

account the results about the derivative of $\mathbf{R}$ (sections B.2 and B.3.1), we finally relate the angular velocity vector $\boldsymbol{\omega}$ to the rotation vector and its first derivative:

$$\boldsymbol{\omega} = \mathbf{H}(\mathbf{r})\dot{\mathbf{r}} \tag{9}$$

where $\mathbf{H}(\mathbf{r}) = \mathbf{I} + g(\theta)\mathbf{X}(\mathbf{r}) + h(\theta)\mathbf{X}(\mathbf{r})^2$, in which $\theta = \|\mathbf{r}\|$, $g(\theta) = (1-\cos\theta)/\theta$, and $h(\theta) = (1 - f(\theta))/\theta^2$.

Substituting equations (8), (9) and (7) into equation (1), we may formulate the kinetic energy in terms of the transformation parameters:

$$E_K = \frac{1}{2}\left(m(S)\,\dot{\mathbf{t}}^2 + \dot{\mathbf{r}}^T\mathbf{H}(\mathbf{r})^T\mathbf{R}\mathbf{J}_0\mathbf{R}^T\mathbf{H}(\mathbf{r})\dot{\mathbf{r}}\right) \tag{10}$$

2.3 Derivatives of the potential energy

The derivative of the potential energy with respect to any parameter q is equal to:

$$\frac{\partial E_P}{\partial q} = \int_S \frac{\partial p(P)}{\partial q} dv(P) = \int_S \boldsymbol{\nabla} p(P).\frac{\partial \overrightarrow{OP}}{\partial q} dv(P) \tag{11}$$

Differentiating equation (6) with respect to the first coordinate of the translation vector t_x, we obtain:

$$\frac{\partial \overrightarrow{OP}}{\partial \mathrm{t}_x} = \mathbf{x}$$

where $(\mathbf{x}, \mathbf{y}, \mathbf{z})$ denotes the coordinate basis. It follows that the derivative of the potential energy with respect to the translation vector is simply:

$$\frac{\partial E_P}{\partial \mathbf{t}} = \begin{pmatrix} \partial E_P / \partial \mathrm{t}_x \\ \partial E_P / \partial \mathrm{t}_y \\ \partial E_P / \partial \mathrm{t}_z \end{pmatrix} = -\mathbf{f}_p \tag{12}$$

where $\mathbf{f}_p = \displaystyle\int_S (-\boldsymbol{\nabla} p(P))\; dv(P)$.

Differentiating equation (6) with respect to the first coordinate of the rotation vector r_x, we obtain (see appendix B):

$$\frac{\partial \overrightarrow{OP}}{\partial \mathrm{r}_x} = \frac{\partial \mathbf{R}}{\partial \mathbf{r}_x}\overrightarrow{G_0P_0} = \mathbf{X}\left(\mathbf{H}(\mathbf{r})\mathbf{x}\right)\mathbf{R}\overrightarrow{G_0P_0} = \left(\mathbf{H}(\mathbf{r})\mathbf{x}\right) \wedge \overrightarrow{GP}$$

Substituting this result into equation (11) yields:

$$\begin{aligned}\frac{\partial E_P}{\partial \mathrm{r}_x} &= \int_S \boldsymbol{\nabla} p(P).\left[(\mathbf{H}(\mathbf{r})\mathbf{x}) \wedge \overrightarrow{GP}\right] dv(P) \\ &= \int_S (\mathbf{H}(\mathbf{r})\mathbf{x}).\left[\overrightarrow{GP} \wedge \boldsymbol{\nabla} p(P)\right] dv(P) = -(\mathbf{H}(\mathbf{r})\mathbf{x}).\mathbf{m}_p(G)\end{aligned}$$

where $\mathbf{m}_p(G) = \int_S \overrightarrow{GP} \wedge (-\boldsymbol{\nabla} p(P))\ dv(P)$. The derivative of the potential energy with respect to the rotation vector is finally:

$$\frac{\partial E_P}{\partial \mathbf{r}} = \begin{pmatrix} \partial E_P / \partial \mathrm{r}_x \\ \partial E_P / \partial \mathrm{r}_y \\ \partial E_P / \partial \mathrm{r}_z \end{pmatrix} = -\begin{pmatrix} (\mathbf{H}(\mathbf{r})\mathbf{x})^T \\ (\mathbf{H}(\mathbf{r})\mathbf{y})^T \\ (\mathbf{H}(\mathbf{r})\mathbf{z})^T \end{pmatrix} \mathbf{m}_p(G) = -\mathbf{H}(\mathbf{r})^T \mathbf{m}_p(G) \qquad (13)$$

2.4 Parametric form of Lagrange equations

Using equations (4), (10), and (12), the Lagrange equations for the three translation parameters are simply:

$$m(S)\ddot{\mathbf{t}} = \mathbf{f}_p \qquad (14)$$

which is Newton's equation (26) since $\ddot{\mathbf{t}} = \boldsymbol{\gamma}(G)$.

Calculating the derivative of the kinetic energy (equation (10)) in the Lagrange equation for the first coordinate of the rotation vector, we obtain:

$$\begin{aligned}\frac{\partial E_K}{\partial \mathrm{r}_x} &= \dot{\mathbf{r}}^T \left(\frac{\partial \mathbf{H}(\mathbf{r})^T}{\partial \mathrm{r}_x}\mathbf{R} + \mathbf{H}(\mathbf{r})^T \frac{\partial \mathbf{R}}{\partial \mathrm{r}_x}\right) \mathbf{J}_0(G_0)\mathbf{R}^T\mathbf{H}(\mathbf{r})\dot{\mathbf{r}} \\ &= \dot{\mathbf{r}}^T \left(\frac{\partial \mathbf{H}(\mathbf{r})^T}{\partial \mathrm{r}_x} + \mathbf{H}(\mathbf{r})^T \mathbf{X}(\mathbf{H}(\mathbf{r})\mathbf{x})\right) \mathbf{R}\mathbf{J}_0(G_0)\mathbf{R}^T\mathbf{H}(\mathbf{r})\dot{\mathbf{r}}\end{aligned}$$

Similarly,

$$\begin{aligned}\frac{\mathrm{d}}{\mathrm{d}t}\left(\frac{\partial E_K}{\partial \dot{\mathrm{r}}_x}\right) &= \frac{\mathrm{d}}{\mathrm{d}t}\left(\mathbf{x}^T\mathbf{H}(\mathbf{r})^T\mathbf{R}\mathbf{J}_0(G_0)\mathbf{R}^T\mathbf{H}(\mathbf{r})\dot{\mathbf{r}}\right) \\ &= \mathbf{x}^T\dot{\mathbf{H}}(\mathbf{r})^T\mathbf{R}\mathbf{J}_0(G_0)\mathbf{R}^T\mathbf{H}(\mathbf{r})\dot{\mathbf{r}} \\ &\quad + \mathbf{x}^T\mathbf{H}(\mathbf{r})^T\mathbf{X}(\mathbf{H}(\mathbf{r})\dot{\mathbf{r}})\mathbf{R}\mathbf{J}_0(G_0)\mathbf{R}^T\mathbf{H}(\mathbf{r})\dot{\mathbf{r}} \\ &\quad + \mathbf{x}^T\mathbf{H}(\mathbf{r})^T\mathbf{R}\mathbf{J}_0(G_0)\mathbf{R}^T\mathbf{X}(\mathbf{H}(\mathbf{r})\dot{\mathbf{r}})^T\mathbf{H}(\mathbf{r})\dot{\mathbf{r}} \\ &\quad + \mathbf{x}^T\mathbf{H}(\mathbf{r})^T\mathbf{R}\mathbf{J}_0(G_0)\mathbf{R}^T\dot{\mathbf{H}}(\mathbf{r})\dot{\mathbf{r}} \\ &\quad + \mathbf{x}^T\mathbf{H}(\mathbf{r})^T\mathbf{R}\mathbf{J}_0(G_0)\mathbf{R}^T\mathbf{H}(\mathbf{r})\ddot{\mathbf{r}}\end{aligned}$$

The latter expression can be simplified by noting that:

- The third term in $\frac{\mathrm{d}}{\mathrm{d}t}\left(\frac{\partial E_K}{\partial \dot{\mathrm{r}}_x}\right)$ disappears since $\mathbf{X}(\mathbf{H}(\mathbf{r})\dot{\mathbf{r}})^T\mathbf{H}(\mathbf{r})\dot{\mathbf{r}} = 0$
- $\dot{\mathbf{H}}(\mathbf{r})\mathbf{x} = \left(\dfrac{\partial \mathbf{H}(\mathbf{r})}{\partial \mathrm{r}_x} + \left(\mathbf{X}(\mathbf{H}(\mathbf{r})\mathbf{x})\right)^T \mathbf{H}(\mathbf{r})\right)\dot{\mathbf{r}}$

Multiplying on the left by $\left(\mathbf{H}(\mathbf{r})^T\right)^{-1}$, Lagrange equations for the three rotation parameters can be written:

$$\mathbf{X}\left(\mathbf{H}(\mathbf{r})\dot{\mathbf{r}}\right)\mathbf{R}\mathbf{J}_0(G_0)\mathbf{R}^T\mathbf{H}(\mathbf{r})\dot{\mathbf{r}} + \mathbf{R}\mathbf{J}_0(G_0)\mathbf{R}^T\dot{\mathbf{H}}(\mathbf{r})\dot{\mathbf{r}} + \mathbf{R}\mathbf{J}_0(G_0)\mathbf{R}^T\mathbf{H}(\mathbf{r})\ddot{\mathbf{r}} = \mathbf{m}_p(G)$$

Equivalently,

$$\mathbf{X}\left(\mathbf{H}(\mathbf{r})\dot{\mathbf{r}}\right)\mathbf{J}(G)\mathbf{H}(\mathbf{r})\dot{\mathbf{r}} + \mathbf{J}(G)\dot{\mathbf{H}}(\mathbf{r})\dot{\mathbf{r}} + \mathbf{J}(G)\mathbf{H}(\mathbf{r})\ddot{\mathbf{r}} = \mathbf{m}_p(G) \tag{15}$$

This is the Euler equation (27) since we have

$$\begin{aligned}\boldsymbol{\delta}(G) &= \dot{\boldsymbol{\sigma}}(G) \quad \text{with} \quad \boldsymbol{\sigma}(G) = \mathbf{J}(G)\boldsymbol{\omega} = \mathbf{J}(G)\mathbf{H}(\mathbf{r})\dot{\mathbf{r}} \\ &= \frac{\mathrm{d}}{\mathrm{d}t}\left(\mathbf{R}\mathbf{J}_0(G_0)\mathbf{R}^T\mathbf{H}(\mathbf{r})\dot{\mathbf{r}}\right)\end{aligned}$$

Adding viscosity dissipation term (see section A.3.2) to Lagrange equations, we finally obtain:

$$\begin{cases} m(S)\left(\ddot{\mathbf{t}} + \dfrac{\kappa}{\rho}\dot{\mathbf{t}}\right) & = \mathbf{f}_p \quad (16a) \\ \left(\mathbf{X}\left(\mathbf{H}(\mathbf{r})\dot{\mathbf{r}}\right) + \dfrac{\kappa}{\rho}\mathbf{I}\right)\mathbf{J}(G)\mathbf{H}(\mathbf{r})\dot{\mathbf{r}} + \mathbf{J}(G)\dot{\mathbf{H}}(\mathbf{r})\dot{\mathbf{r}} + \mathbf{J}(G)\mathbf{H}(\mathbf{r})\ddot{\mathbf{r}} & = \mathbf{m}_p(G) \quad (16b) \end{cases}$$

2.5 Minimization of potential energy

To find a minimum of the potential energy E_P of the moving solid S, we discretize equation (16) in time, choosing an appropriately small time step dt, and iterate until the system stabilizes.

2.5.1 Potential and force fields

We suppose that the reference object R generates a potential field p whose value at point P is:

$$p(P) = \frac{d(P,R)^2}{2}$$

where $d(P,R)$ denotes the distance from P to the closest point in R. The distance field d of R can be estimated and pre-computed using chamfer distances [7], then the value of the force field at P is given by $-d(P,R)\nabla d(P,R)$.

One may pre-compute the force field instead of the distance field. If all the points of an open neighborhood of P have the same closest point Q in R, then $-d(P,R)\nabla d(P,R) = \overrightarrow{PQ}$. This last vector field can be calculated with euclidean distance mapping methods [15]. The potential value at P may then be estimated by: $p(P) = \frac{\|\overrightarrow{PQ}\|^2}{2}$

If the number of points of R is not too large, they can be stored in a pre-computed structure, for instance a Kd-tree [54], and the force acting can be calculated efficiently.

2.5.2 Euler methods

One of the most common ways to discretize equations in time is to use explicit Euler methods, as follows

- $\ddot{q}_t \approx \frac{q_{t+dt} - 2q_t + q_{t-dt}}{dt^2}$: central-point update rule
- $\dot{q}_t \approx \frac{q_t - q_{t-dt}}{dt}$: left-point update rule
- initial values of q are: $q_{-dt} = q_0$

Considering equation (16a), we obtain the following translation update rule:

$$\mathbf{t}_{t+dt} \approx \mathbf{t}_t + (\mathbf{t}_t - \mathbf{t}_{t-dt})(1 - \frac{\kappa}{\rho}dt) + \frac{dt^2}{m(S)}\,\mathbf{f}_p$$

which can be compared to the steepest-descent approach (recall that $\frac{\partial E_P}{\partial \mathbf{t}} = -\mathbf{f}_p$):

$$\mathbf{t}_{t+dt} \approx \mathbf{t}_t \qquad\qquad + \lambda\,\mathbf{f}_p$$

The additional term $(\mathbf{t}_t - \mathbf{t}_{t-dt})(1 - \frac{\kappa}{\rho}dt)$ allows one:

1. to speed up the convergence of the minimization,
2. to avoid some local minima of the potential energy.

This comparison shows the advantages of the dynamic character of a Lagrangian approach over a steepest-descent-like approach.

2.5.3 Taylor expansion

Instead of using Euler methods, we update the transformation parameters by a Taylor expansion, i.e.:

$$\left\{ \begin{array}{rcccccc} \mathbf{t}_{t+dt} & \approx & \mathbf{t}_t & + & \dot{\mathbf{t}}_t & + & \ddot{\mathbf{t}}_t \frac{dt^2}{2} \\ \mathbf{r}_{t+dt} & \approx & \mathbf{r}_t & + & \dot{\mathbf{r}}_t & + & \ddot{\mathbf{r}}_t \frac{dt^2}{2} \end{array} \right. \tag{17}$$

in which $\ddot{\mathbf{t}}_t$ and $\ddot{\mathbf{r}}_t$ are given by equation (16). Update rules for the first derivatives of both $\mathbf{t}$ and $\mathbf{r}$ are:

$$\left\{ \begin{array}{rcccc} \dot{\mathbf{t}}_{t+dt} & \approx & \dot{\mathbf{t}}_t & + & \ddot{\mathbf{t}}_t dt \\ \dot{\mathbf{r}}_{t+dt} & \approx & \dot{\mathbf{r}}_t & + & \ddot{\mathbf{r}}_t dt \end{array} \right. \tag{18}$$

Initial values of the first derivatives are set to zero: $\dot{\mathbf{t}}_0 = \dot{\mathbf{r}}_0 = \vec{0}$. The experiments we have carried out, see section 3, suggest strongly that update rules derived from the Taylor expansion perform better than those derived from Euler methods, for the minimization scheme we propose below.

2.5.4 Energy dissipation

To ensure the convergence of the potential minimization, an energy dissipation term was added to Lagrange equation (see equations (16)). The question is how to choose the viscosity κ. One may choose it either to be constant or to depend on time: for example, to be small at the beginning and large at the end [58].

Instead (consider now equations (16) with $\kappa = 0$), we develop minimization heuristics and abruptly decrease the energy at certain times by setting the first temporal derivatives of the transformation parameters (i.e. the kinetic energy, see equation (10)) to $\vec{\mathbf{0}}$ (see figure 1). The times where we abruptly decrease the energy are those defining a minimum of the potential energy, which may be the first encountered potential minimum (see figure 2) or not (see figure 3). Effectively, the first encountered potential minimum may or may not be the global minimum, i.e. the right position of registration. Looking further than this first minimum enables the algorithm more often to avoid local minima.

The two previous heuristics are convenient if the moving object S is a subset (in the registration position) of the reference object R. However, as occlusions or unavoidable errors in the preprocessing of the image (e.g. segmentation) may occur, we present in figure 4 a modified version of heuristic of figure 2 which can reject outliers: points "too far away" from the reference object R are rejected for the computation of both the force and the torque.

1. At the k^{th} iteration, consider the moving solid S to be motionless (the first temporal derivatives of the transformation parameters are set to zero);
2. compute a new transformation which gives a $(k+1)^{th}$ position of S minimizing its potential energy:
   (a) if the found transformation is the same as the one giving the k^{th} position, (the potential energy can not be minimized), consider smaller displacements by decreasing the value of dt: if dt becomes too small, then stop the algorithm,
   (b) return to step 1 with the new position of S or the new value of dt.

Figure 1: Minimization algorithm.

1. At time t, compute the force $\mathbf{f}_p$ and the torque $\mathbf{m}_p(G)$ acting on the solid S;
2. compute the parameters of the transformation to reach the new position of S at time $t+dt$ and update their first temporal derivatives at time $t+dt$ with equations (17) and (18);
3. compare the potential energies E_P at times t and $t+dt$:
   (a) if $E_P(t+dt) < E_P(t)$, the motion is directed towards a minimum, proceed to step 1 with $t = t+dt$.
   (b) if $E_P(t+dt) \geq E_P(t)$, S has crossed a local minimum; the transformation sought is the previous one (the one to reach the position at time t).

Figure 2: Heuristic to find a transformation which minimizes the potential energy by studying a solid motion. The search stops at the first encountered local minimum.

1. At time t, compute the force $\mathbf{f}$ and the torque $\mathbf{m}(G)$ acting on the solid S;
2. compute the parameters of the transformation to reach the new position of S at time $t + dt$ and update their first temporal derivatives at time $t + dt$ with equations (17) and (18);
3. compare the potential energies E_P at times $t - dt$, t and $t + dt$:
   (a) if $E_P(t)$ is a local minimum of potential,
      i. if a previous minimum has already be found, then keep the one with the smallest potential energy;
      ii. else keep this one as *a priori* minimum;
   (b) else let the motion continue;
4. the end condition of this heuristic is more elaborate than the one of figure 2: stop after a *given amount of time*, which may either be a constant or depend on the first encountered minimum.

Figure 3: Heuristic to find a transformation which minimizes the potential energy by studying a solid motion. The search does not stop at the first encountered local minimum.

1. At time t, we compute a threshold from the histogram of the distances between the moving object S and the reference solid R; the force $\mathbf{f}_p$ and the torque $\mathbf{m}_p(G)$ acting on the solid S are computed for points whose distance to R is less than this threshold.
2. same as in figure 2;
3. same as in figure 2.

Figure 4: Heuristic to find a transformation which minimizes the potential energy by studying a solid motion. The search stops at the first encountered local minimum of potential, but some points are rejected.

As three heuristics are proposed for the minimization process, the question is how do we use them all efficiently. We propose the following order:

1. if the initial position is far from the registration position, perform several iterations of the general algorithm using the heuristic of figure 3;
2. use the heuristic of figure 2 until convergence;
3. eventually (if the distribution of distances let us suppose that outliers or occlusions may exist), use the heuristic of figure 4 in the general algorithm until convergence.

In previous conference publications [41, 42], only the heuristic of figure 2 (the step 2 of the above method) was proposed. The two additional heuristics make the method more robust to local minima of the potential and to outliers or segmentation errors.

3 A synthetic example

We illustrate a number of issues by showing a synthetic example with local minima.

3.1 Description of the test

Consider two objects on the real line, $M = \{-d, 0, d\}$ and $S(x) = \{-d+x, x, d+x\}$, made of 3 equally spaced points, which are to be registered with only one degree of freedom x (a translation along an axis). This gives a potential energy curve as described above (see figure 6): there is a global minimum for $x = 0$, two local minima for $x \in \{-0.66d, 0.66d\}$, and two local maxima ($E_p = 0.375d^2$) for $x \in \{-0.5d, 0.5d\}$ corresponding to discontinuities of the potential energy derivative (see figure 7).

Because of the symmetry in the example, we only discuss the case $x < 0$ in the following. Of course, if the initial position x_0 is such that $x_0 < -0.5d$ and $E_p(S(x_0)) < 0.375d^2$ (the potential energy of the local maxima) any classical registration method will be trapped by the local minimum at $-0.5d$.

The potential energy $0.375d^2$ is obtained for $x \in \{-5/6d, 5/6d\}$ too.

3.2 Sensitivity to local minima

As discussed above, local minima occurs only for $x < -5/6d$. We have compared the following algorithms: least squares minimization [6], steepest-descent [55], another

type of descent (opposite inverse of the Hessian multiplied by the gradient) [55], Levenberg-Marquardt [37] and our method (using two kinds of update rules: Euler methods and Taylor expansions).

We tested several intervals of initial positions (for instance, 4167 initial positions from $-5d$ to $-5/6d$ with a step of $0.001d$ or 9167 initial positions from $-10d$ to $-5/6d$ with the same step). The four classical minimization algorithms are always trapped by the local minimum at $x = -0.66d$, but the proposed heuristic method (with $dt = 1$, and Taylor expansion update rules) finds the global minimum with a high percentage of success (see tables 1 and 2).

This result derives from the fact that the other methods consider only the potential energy and so they are trapped by the first minimum of this energy. On the contrary, our method considers both potential and kinetic energies, and the whole energy can be larger than the local maximum energy and the motion can cross over this local maximum. This is illustrated in figure 8.

The percentage failure (in this case) is not null, we note that:

1. As does any iterative method, its result still depends on the initial position of the moving object.

2. All iterative methods set some parameters, and we have to set the value of the time interval dt. In this test and in our practical experiments, its initial value is 1, although the second order evolution of the transformation parameters (17) stands only for small values of dt.

   - On one hand, setting dt to a large value increases artificially the kinetic energy of the moving solid, then it can not only more easily *jump over* the local maxima of the potential energy, but also escape from inside a local minima (see the first column of table 2: the energy of the initial position is less than the one of the local maxima).
   - On the other hand, it may cause a too large displacement of the moving object in the neighborhood of the global minimum (and then we may miss it).

3. According to the previous remark, further work on the behavior of our method with respect to dt has to be done.

Considered interval	$[-5/6d, -0.5d]$	$[-5d, -5/6d]$	$[-10d, -5/6d]$	$[-11d, -10d]$	$[-20d, -10d]$
Study step	$0.001d$	$0.001d$	$0.001d$	$0.001d$	$0.001d$
Number of trials	334	4167	9167	1000	10000
Successful trials (Taylor expansion)	0	3552	7829	1000	8553
Success rate (Taylor expansion)	0.00 %	85.24 %	85.40 %	100.00 %	85.53 %
Successful trials (Euler methods)	0	3777	8777	1000	10000
Success rate (Euler methods)	0.00 %	90.64 %	95.75 %	100.00 %	100.00 %

Table 1: Success rates for the minimization algorithm of figure 1 using the heuristic of figure 2, with $dt = 1$, for both Taylor expansion and Euler method update rules.

Considered interval	$[-5/6d, -0.5d]$	$[-5d, -5/6d]$	$[-10d, -5/6d]$	$[-11d, -10d]$	$[-20d, -10d]$
Study step	$0.001d$	$0.001d$	$0.001d$	$0.001d$	$0.001d$
Number of trials	334	4167	9167	1000	10000
Successful trials (Taylor expansion)	333	4165	9158	1000	9995
Success rate (Taylor expansion)	99.70 %	99.95 %	99.90 %	100.00 %	99.95 %
Successful trials (Euler methods)	135	3968	8968	1000	10000
Success rate (Euler methods)	40.42 %	95.22 %	97.83 %	100.00 %	100.00 %

Table 2: Success rates for the minimization algorithm of figure 1 using the heuristic of figure 3, with $dt = 1$, for both Taylor expansion and Euler method update rules.

3.3 Comparison of Euler methods versus Taylor expansion

We presented in section 2.5, two kinds of update rule, Euler methods and Taylor expansions.

Tables 1 and 2 give a preliminary comparison between the two kinds of update rules. In this simple test, it seems that the Euler method performs better than the Taylor expansion, at least for the heuristic of figure 2. On the contrary, Taylor expansions perform better with the heuristic of figure 3, especially when the start point is inside a local minima.

We can explain that behavior, The Euler method seems to under-evaluate the kinetic energy (see figure 10), so minimization with such method is less likely to escape from the nearest minimum. As heuristic of figure 2 stops at the first encountered minimum, the Euler method is more adapted to that heuristic. On the other hand, the Taylor expansion seems to over-evaluate the kinetic energy (see figure 11), and so minimization with such a method is more likely to escape from the nearest minimum. As heuristic of figure 3 does not stop at the first encountered minimum, the Taylor expansion is more adapted to that particular heuristic.

Thus, as we begin the minimization with several iterations using the heuristic of figure 3, we use update rules deriving from the Taylor expansion.

4 Results

We present results from our primary application, the registration of multi-modality medical images. We use the heuristics and the algorithm presented in section 2.5 with an initial value of dt equal to 1; in step 2a of the general algorithm (see figure 1), we decrease dt by dividing it by 2 and we stop the algorithm if dt becomes smaller than 0.1.

The segmentation of the brain in MRI images uses an analysis of the grey-level histogram to determine thresholds for the brain [10], and mathematical morphology to perform the complete segmentation [10, 39]. The segmentation of the brain in metabolic images uses an analysis of the grey-level histogram to determine a single threshold [25]: points whom value is upper this threshold are assumed to belong to the brain. For the matching, we use the whole segmented volume instead of the surface.

4.1 MRI images of the brain

We have two MRI images of the same patient head, taken at different dates. They have respectively 54 and 51 slices of 256x256 voxels. The voxel size is 0.94x0.94x3 mm^3. Some slices of the original images can be seen in figures 12 and 13. We can easily extract the brain from both images by using mathematical morphology (see [39]). We compute the registration with both brains and apply the found transformation in order to resample one of the images. We show in figure 14 a slice of the second image after resampling, corresponding to one of figure 12.

Now if we look carefully at this slice in figure 12, 13 and 14, we can see in the first original brain a thin black structure (the middle cerebral artery) which does not appear completely in the corresponding slice of the second original data. If one looks at the corresponding slice of the resampled image (figure 14), one can see now this whole artery.

We present in figure 14 the superimposition of edges extracted from the central slice of figure 12 on the corresponding resampled slice after registration.

To be more convincing, we present sagittal and coronal slices of the two original images and of the resampled one in figures 15 and 16.

These figures seem blurred because we resampled them a second time along the vertical axis in order to obtain quasi-isotropic voxels, for display purpose only.

4.2 Brain: PET-MRI registration

We have an MRI image of size 256x256x120 of the brain with voxels of size 1.3x1.3x1.3 mm^3 and no inter-slice distance (acquired on a Signa-Advantage 1.5 T). We have extracted the brain with a semi-automatic algorithm, using 3-D mathematical morphology operators [30, 39].

We also have a PET image of size 256x256x7 of the same brain with voxels of size 1x1x9 mm^3 and an inter-slice distance of 3 mm (acquired on a TTV03). These data are obviously anisotropic. As the PET image shows the brain metabolism, we can extract the brain by thresholding.

After registration, we present the superimposition of the seven PET slices on six of the 120 MRI slices in figure 17. Notice the typical orientation of the PET slices with respect to the sagittal views due to the acquisition procedure.

The registration takes 134 seconds CPU on a DEC 5000 workstation. We resampled the MRI slices corresponding to PET ones, extracted the edges of these resampled slices with a classical algorithm [48] and superimposed them with original PET slices in figure 18.

With this method, we obtain anatomical information superimposed on the functional one.

4.3 Brain: SPECT-MRI registration

In practice, one may not have the good quality images presented in the above example. We now show an MRI image of size 256x256x12 of the brain with voxels of size 1.033x1.033x10 mm^3 with an inter-slice distance of 2 mm. We have extracted the brain with a semi-automatic algorithm, using mathematical morphology operators. As slices are very thick, we did not use a 3-D algorithm as in the previous example but a 2-D one which was applied on each slice.

We also have a SPECT image of size 64x64x25 of the same brain with voxels of size 3.2x3.2x6.4 mm^3 and no inter-slice distance. As the SPECT image shows the brain metabolism, we can easily extract the brain by thresholding.

After registration, we resampled the SPECT slices corresponding to MRI ones, extracted the edges of the original MRI slices and superimposed them with resampled SPECT slices in figure 19.

With this method, we obtain anatomical information superimposed on the functional data.

5 Further developments

5.1 Resampling of the moving object S

In our experiments on real medical images, the initial position given by identifying the acquisition axis (we assume that we know the acquisition geometry) was always sufficient to register our images.

However, in other applications, such an initial position may not be known. In this case, several initial positions have to be tested, and it then becomes important to decrease the computational cost of the matching process while keeping a good quality registration.

This computational cost is directly linked to the number of points of the moving object S because of the computation of both the force and the torque (see section A.3). For that purpose, we have to create a resampled representation of the moving object, and eventually (for a hierarchical approach) of the reference object (or of the associated potential field) [22].

5.1.1 Uniform subsampling

We collect a block of $\mathbf{b}_x.\mathbf{b}_y.\mathbf{b}_z$ voxels from the initial image in order to create a new voxel in the resampled moving object. The change of resolution need not be the same along each axis.

As S is considered to be a solid, an elementary volume is attached to any point to make the computations connected to the solid. This elementary volume is linked to the elementary point mass thanks to the density ρ. We must take care of preserve the inertia parameters of S: the whole volume (i.e. the whole mass), the center of mass, and the inertia tensor. So, we assign to the new voxel (the block of $\mathbf{b}_x.\mathbf{b}_y.\mathbf{b}_z$ voxels) a volume equal to the sum of elementary volumes of S voxels in this block.

But, this method of resampling shifts the center of mass of the solid: the center of mass of some points in a $\mathbf{b}_x.\mathbf{b}_y.\mathbf{b}_z$ block is not found in the center of block.

Thus, the resampling operation does not transform the original image into an other image (i.e. a subset of $\mathbb{Z}^3$) but into a list of points with real coordinates (the coordinates of the center of mass of the block points) associated with a volume.

Therefore the whole volume and the center of mass of the start image are still the same in the resampled list.

The last inertia parameter we must take care of is the inertia tensor. It is obvious that the inertia matrix of the resampled list is not that of the start object S. However, as we have to examine all the points of the initial image in order to build a resampled list, we can compute at the same time the inertia matrix of S and use it for subsequent computation.

Then, we make sure that the inertia parameters are preserved. Results of such a subsampling are presented in figure 21.

5.1.2 Octree-like subsampling

In the subsampling method presented above, the precision of the registration decreases with the size of the block of voxels, because the geometry of the object is perturbed.

What we want in fact is a process which approximately preserves the geometry of the object, an adaptive subsampling. This will transform a $\mathbf{b}_x.\mathbf{b}_y.\mathbf{b}_z$ block of voxels into a big voxel if and only if all the voxels of this block belong to the moving object; if not, the block is divided into eight sub-blocks (or four for a quadtree-like subsampling) and each of these sub-blocks are examined in the same way.

In this way, we preserve a good quality registration, because we maintain a large number of points on the object border. Several results of such a subsampling are presented in figure 22.

5.1.3 Kdtree-like subsampling

We may decrease the number of points relative to the last method, by changing the subdivision of a block. Instead of dividing it into eight (or four) sub-blocks, we split it only in two along one dimension (then sub-blocks may be divided again along the next dimension). Results of such a subsampling are presented in figure 23.

These last two methods of adaptive subsampling of the moving object yield globally the same results as with the original object.

5.2 Resampling of the reference object R

A purely hierarchical approach needs to resample both the moving object and the reference object. We already presented a uniform subsampling of the moving object in section 5.1.1. A uniform subsampling of the reference object can be achieved:

- by subsampling the original binary image enclosing the reference object: a voxel of the subsampled image (i.e. a block of $\mathbf{b}_x.\mathbf{b}_y.\mathbf{b}_z$ voxels of the original image) belongs to the subsampled reference object if at least one of the $\mathbf{b}_x.\mathbf{b}_y.\mathbf{b}_z$ voxels belongs to the original reference object. This approach is recommended by Borgefors [8] who claimed that undersampling of the distance map does not preserve the minima (she averages the values of the $\mathbf{b}_x.\mathbf{b}_y.\mathbf{b}_z$ voxels in the distance map). On the other hand, one needs to compute a distance map for each level of subsampling.

- by directly subsampling the distance map of the original reference object. Instead of averaging distances in the block of $\mathbf{b}_x.\mathbf{b}_y.\mathbf{b}_z$ voxels, we consider the minimum of the distances in this block: it will give us the minimum distance of this block to the closest reference object point. In this way, one needs compute only one distance map (at the finer level) and to deduce from it the distance maps at coarser levels.

We have to remark that there exist other approaches that yield an adaptive distance map which is more detailed in the vicinity of the motionless solid than far away from it (octrees-splines, [37]).

5.3 Multi-potentials minimization

Iterative methods of matching are useful when we do not have point-to-point correspondences between both objects to register. However, we can take advantage of the fact that, in the two objects, there are sets of points that have the same features (geometrical or topological properties): for instance, in case of complex 3-D objects made of surfaces, we may distinguish surface points from junction points (see [40]).

We first classify points of both objects before the matching process. Each class of the motionless object will generate a separate distance map. Points of each moving object class will be attracted by points of the same class: it means there is a different force field associated with each class of points. Our experiments show that this multi-potential minimization gives more accurate results and allows some local minima to be avoided [22].

6 Accuracy of the registration

The problem is: how to measure the accuracy of the registration, considering that we do not have a point-to-point correspondence ?

If some marks are available for registering both images, one may first segment them and second register them to obtain a rigid transformation with an associated error (due to the acquisition, the segmentation and the registration processes): the registration error of the tested method cannot be estimated under this first error.

Instead of marks, one may use a reference matching algorithm where the final error is known [53, 65]: the algorithm referenced here is based on crest lines, but it works only for good quality and high resolution monomodal images, like the ones presented in section 4.1. The differences between our method and the one referenced are, on this example, less than one millimeter for the translation and less than one degree for the rotation.

Another way to estimate the accuracy of the registration is to apply a first rigid transformation to a known object and to try to recover this transformation by register the original object with the transformed one. We apply such a scheme in [43] with a synthetic object and a set of several transformations and recover the searched transformation with a precision under the voxel for the translation (and it is difficult to estimate this precision under the voxel because of the error due to the segmentation process), and under the degree for the rotation if the initial rotation angle is lower than 30 degrees (for superior angles, false matching may appear in our experiments).

These experiments seem to indicate a high accuracy of our registration method. However, since they depend on a first estimate of the registration, they are not totally reliable.

A more correct way to estimate the accuracy of a registration could be the following: to scan a given object to obtain a first image, then to apply to it a given rigid transformation precisely measured and to scan it again: as the transformation is directly measured and not estimated, it can be considered as correct; however, the acquisition conditions have to be identical for both scans.

Unfortunately, we do not have access to such data, but this could be the topic of a further work.

7 Conclusion

We present a new iterative matching algorithm between 3-D objects. The principle of our method is an application of the fundamental laws of dynamics.

A synthetic example shows the usefulness of such a method by demonstrating its ability to avoid local minima: it derives from the fact we consider not only the potential but also the kinetic energy.

In the medical imaging field, this method can be used for registration either between mono-modality or multi-modalities images. Instead of using only the surface of the segmented objects for matching, we use the whole segmented volume. To keep a reasonable computational cost, we present some subsampling methods adapted to our approach. Results on real images have shown the accuracy and the utility of the method.

Although the presented results are promising, this method and its study have to be more developed. Our future work will include the study of the accuracy of the final registration and of the behavior of the method with respect to local minima in more complex situations than the one presented in section 3.

This method, combined to a segmentation method, is about to be marketed by Focus-Medical (Grenoble, France) for medical applications.

Acknowledgment

This work was partially supported by Digital Equipment Corporation. We thank Dr. Jael Travere (Cyceron center, CEA, Caen, France), Philippe Boulle (Focus-Medical, Grenoble, France), Ron Kikinis, M.D., (Brigham and Women's Hospital, Boston, USA) and GE-MS (Buc, France) for providing medical data. Special thanks are due

to professor Mike Brady, Hervé Delingette and Nicholas Ayache for a substantial help in the redaction of this paper.

A Recalls of kinematics and dynamics

A.1 Center of mass and inertia tensor

Consider a 3-D solid S. Associate with any point P of the solid S, a mass density $\rho(P)$ and an elementary volume $dv(P)$. Denote by $dm(P)$ the elementary mass $\rho(P)\, dv(P)$ associated with each point P. In the following, we assume that the density of S is constant and equal to ρ.

By definition of the solid, the euclidean distance between any two solid points, the density and the elementary volume of each point P are constant. The solid may be partially described by its *center of mass* (or centroid) and its *inertia tensor* (or inertia matrix), a 3×3 matrix which characterizes the distribution of mass of the solid.

The center of mass G of the solid S can be computed by:

$$\int_{P \in S} P\, dm(P) = m(S)\; G \quad \text{with} \quad m(S) = \int_{P \in S} dm(P) \tag{19}$$

where $m(S)$ is the mass of the solid S.

The inertia tensor $\mathbf{J}$ of the solid S is computed with respect to an arbitrary point Q. If (x, y, z) are the coordinates of the vector $\overrightarrow{QP}$ in an orthonormal basis (X, Y, Z), we have:

$$\mathbf{J}(Q) = \begin{bmatrix} \displaystyle\int_{P \in S} (y^2 + z^2)\, dm(P) & \displaystyle -\int_{P \in S} xy\, dm(P) & \displaystyle -\int_{P \in S} zx\, dm(P) \\ \displaystyle -\int_{P \in S} xy\, dm(P) & \displaystyle \int_{P \in S} (z^2 + x^2)\, dm(P) & \displaystyle -\int_{P \in S} yz\, dm(P) \\ \displaystyle -\int_{P \in S} zx\, dm(P) & \displaystyle -\int_{P \in S} yz\, dm(P) & \displaystyle \int_{P \in S} (x^2 + y^2)\, dm(P) \end{bmatrix}$$

The integrals in $\mathbf{J}$ are three-dimensional integrals over the volume V occupied by the solid. $\mathbf{J}$ is a symmetric matrix containing six independent terms. The three diagonal terms of the matrix are called the moments of inertia, while the three off-diagonal terms are called products of inertia.

The eigenvectors of the inertia matrix are the principal axes of the solid S and the eigenvalues are the principal moments of inertia.

This matrix corresponds to a linear mapping:

$$\mathbf{u} \overset{\mathbf{J}(Q)}{\longmapsto} \int_S \overrightarrow{QP} \wedge (\mathbf{u} \wedge \overrightarrow{QP})\; dm(P)$$

According to the generalized Huyghens theorem, the inertia tensor can be computed with respect to any point and in particular to the center of mass G, thanks to:

$$\mathbf{J}(Q) = \mathbf{J}(G) + \mathbf{J}(Q, \{G, m(S)\}) \tag{20}$$

where $\mathbf{J}(Q, \{G, m(S)\})$ is the inertia matrix with respect to the point Q of the point G with a mass $m(S)$.

A.2 Kinematics

Consider a point P of the solid S. This point has a velocity $\mathbf{v}(P)$ and an acceleration $\boldsymbol{\gamma}(P)$ which are defined by:

$$\mathbf{v}(P) = \dot{P} \qquad \boldsymbol{\gamma}(P) = \ddot{P}$$

where the dot and the double dot denote the first and the second derivative with respect to the time.

A.2.1 Velocities

The velocity of the center of mass is given by the differentiating of equation (19):

$$m(S)\mathbf{v}(G) = \int_{P \in S} \mathbf{v}(P)\, dm(P) \tag{21}$$

Let $(\boldsymbol{\omega}, \mathbf{v}(Q))$ be the kinematic screw of S at Q ($\boldsymbol{\omega}$ is called the angular velocity vector of the solid S), and P a point of S. According to the velocities composition rule, we have:

$$\mathbf{v}(P) = \mathbf{v}(Q) + \boldsymbol{\omega} \wedge \overrightarrow{QP}$$

In particular, we obtain for $Q = G$

$$\mathbf{v}(P) = \mathbf{v}(G) + \boldsymbol{\omega} \wedge \overrightarrow{GP} \quad \forall P \in S \tag{22}$$

The kinetic moment of S, with respect to a point Q, is defined by:

$$\boldsymbol{\sigma}(Q) = \int_{P \in S} \overrightarrow{QP} \wedge \mathbf{v}(P)\, dm(P)$$

The general expression of the kinetic moment of S is rather complicated, but some terms cancel out when expressed with respect to the center of mass G (using equation (22)), and it becomes:

$$\boldsymbol{\sigma}(G) = \mathbf{J}(G)\boldsymbol{\omega} \tag{23}$$

The kinetic energy E_K of S is:

$$E_K = \frac{1}{2}\left(m(S)\,\mathbf{v}(G)^2 + \boldsymbol{\omega}.\mathbf{J}(G)\boldsymbol{\omega}\right)$$

A.2.2 Accelerations

The acceleration of the center of mass is given by differentiating equation (19) twice:

$$m(S)\boldsymbol{\gamma}(G) = \int_{P\in S} \boldsymbol{\gamma}(P)\,dm(P) \tag{24}$$

The dynamic moment of S, with respect to a point Q, is defined by:

$$\boldsymbol{\delta}(Q) = \int_{P\in S} \overrightarrow{QP} \wedge \boldsymbol{\gamma}(P)\,dm(P)$$

We give here an expression for the dynamic moment of S with respect to the center of mass G:

$$\boldsymbol{\delta}(G) = \dot{\boldsymbol{\sigma}}(G) \tag{25}$$

Note that the dynamic moment is generally not equal to the derivative of the kinetic moment, when both moments are expressed with respect to an other point than the center of mass.

A.3 Force and torque

A.3.1 Force field deriving from a potential field

Any potential field p induces a force field expressed by $-\boldsymbol{\nabla}p(P)$ where $\boldsymbol{\nabla}$ is the gradient operator. We may then define the whole force $\mathbf{f}_p$ and the torque $\mathbf{m}_p$ due to the potential field acting on the solid S:

$$\left\{\begin{array}{lcl} \mathbf{f}_p & = & \displaystyle\int_S (-\boldsymbol{\nabla}p(P))\;dv(P) \\ \mathbf{m}_p(Q) & = & \displaystyle\int_S \overrightarrow{QP} \wedge (-\boldsymbol{\nabla}p(P))\;dv(P) \end{array}\right.$$

A.3.2 Viscosity field

Energy dissipation can easily be introduced by adding a viscosity term. Let κ be the viscosity constant, the viscosity force field is expressed by $-\kappa\mathbf{v}(P)$. The whole force

$\mathbf{f}_v$ and the torque $\mathbf{m}_v$ due to the viscosity are:

$$\begin{cases} \mathbf{f}_v & = & -m(S)\dfrac{\kappa}{\rho}\mathbf{v}(G) \\ \mathbf{m}_v(Q) & = & -\dfrac{\kappa}{\rho}\boldsymbol{\sigma}(G) \end{cases}$$

A.3.3 Newton-Euler equations

Newton's equation (26) relates the linear acceleration of the center of mass G to the whole force $\mathbf{f}$ acting on the solid S, whereas the Euler equation (27) relates the dynamic moment to the torque $\mathbf{m}(Q)$ acting on S.

$$\mathbf{f} = m(S)\,\boldsymbol{\gamma}(G) \quad (26)$$

$$\mathbf{m}(Q) = \boldsymbol{\delta}(Q) \quad (27)$$

B Rotation

We recall some properties of rotations (see [2] for more details).

Any rotation in $\mathbb{R}^3$ can be represented by an orthogonal 3×3 matrix $\mathbf{R}$ with determinant equal to 1, that is:

$$\mathbf{R}^T\mathbf{R} = \mathbf{I} \quad \text{and} \quad \det(\mathbf{R}) = 1$$

A rotation can be represented by 3 parameters; some parametrizations are:

unit quaternions : since quaternions are a four-parameter non-minimal representation of rotation, a constraint on the norm is added;

Euler angles : the rotation is decomposed into the product of three rotations of a predefined fixed coordinate system about the axes;

rotation vector : the direction of the vector gives the axis of the rotation whereas its norm gives the angle.

Quaternions provide an explicit solution to minimization problems where a point-to-point correspondence is known [6, 20], but need an additional constraint. Rotations represented by Euler angles are not differentiables for the *pitch* angle β equal to $\pm\pi/2$. Since the rotation vector does not suffer from these disadvantages and seems more appropriate for our purpose, we choose it as representation of rotation.

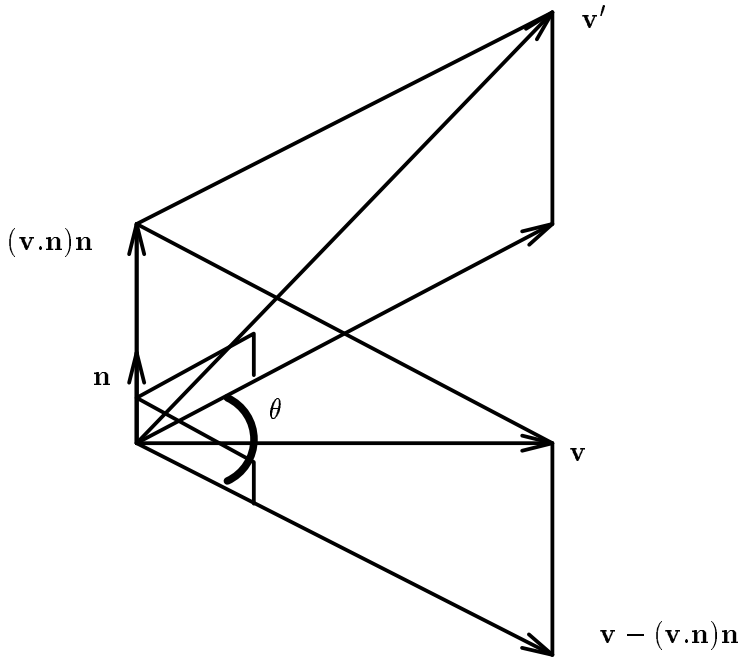

Figure 5: Geometrical representation of the rotation

B.1 Representation by rotation vector [2]

Any rotation $\mathbf{R}$ in $\mathbb{R}^3$ has an invariant axis with normal unit direction vector $\mathbf{n}$, say. Vectors collinear with $\mathbf{n}$ are invariant under $\mathbf{R}$, while orthogonal vectors undergo a rotation of some angle θ in a plane orthogonal to $\mathbf{n}$. $\mathbf{R}$ is represented by $\theta\mathbf{n}$.

Consider figure 5, which shows the image $\mathbf{u}'$ of a vector $\mathbf{u}$ rotated by $\mathbf{R}$ about axis $\mathbf{n}$ through angle θ. We may decompose $\mathbf{u}$ into

$$\mathbf{u} = (\mathbf{u}.\mathbf{n})\mathbf{n} + (\mathbf{u} - (\mathbf{u}.\mathbf{n})\mathbf{n})$$

The first term, collinear to $\mathbf{n}$ is invariant under $\mathbf{R}$, whereas the second, which belongs to the plane orthogonal to $\mathbf{n}$, undergoes a planar rotation through angle θ which may be written:

$$\cos\theta\,(\mathbf{u} - (\mathbf{u}.\mathbf{n})\mathbf{n}) + \sin\theta\,(\mathbf{n} \wedge (\mathbf{u} - (\mathbf{u}.\mathbf{n})\mathbf{n}))$$

This gives:

$$\mathbf{u}' = \cos\theta\,\mathbf{u} + \sin\theta\,\mathbf{n} \wedge \mathbf{u} + (1 - \cos\theta)(\mathbf{u}.\mathbf{n})\mathbf{n}$$

From $\mathbf{n} \wedge (\mathbf{n} \wedge \mathbf{u}) = (\mathbf{n}.\mathbf{u})\mathbf{n} - \mathbf{u}$, we obtain

$$\mathbf{u}' = \mathbf{u} + \sin\theta\,\mathbf{n} \wedge \mathbf{u} + (1 - \cos\theta)\mathbf{n} \wedge (\mathbf{n} \wedge \mathbf{u})$$

Thus the rotation $\mathbf{R}$ may be written (Rodrigues' formula)

$$\mathbf{R} = \mathbf{I} + (\sin\theta)\mathbf{X}(\mathbf{n}) + (1 - \cos\theta)\mathbf{X}(\mathbf{n})^2 \tag{28}$$

where $\mathbf{X}(\mathbf{n})$ is a matrix operator which corresponds to vector product by $\mathbf{n}$, i.e., the antisymmetric matrix formed from the components $(\mathrm{n}_x, \mathrm{n}_y, \mathrm{n}_z)$ of $\mathbf{n}$

$$\mathbf{X}(\mathbf{n}) = \begin{pmatrix} 0 & -\mathrm{n}_z & \mathrm{n}_y \\ \mathrm{n}_z & 0 & -\mathrm{n}_x \\ -\mathrm{n}_y & \mathrm{n}_x & 0 \end{pmatrix}$$

which allows $\mathbf{n} \wedge \mathbf{u}$ to be written as the matrix product $\mathbf{X}(\mathbf{n})\mathbf{u}$.

Any vector $\mathbf{r} \in \mathbb{R}^3$ defines a rotation $\mathbf{R}$ with

$$\theta = \|\mathbf{r}\| \quad ; \quad \mathbf{n} = \frac{\mathbf{r}}{\|\mathbf{r}\|}$$

$\mathbf{R}$ is then written:

$$\mathbf{R} = \mathbf{I} + f(\theta)\mathbf{X}(\mathbf{r}) + g(\theta)\mathbf{X}(\mathbf{r})^2 \tag{29}$$

in which $f(\theta) = \dfrac{\sin\theta}{\theta}$ and $g(\theta) = \dfrac{1 - \cos\theta}{\theta^2}$.

B.2 Derivative of rotation [2]

Proposition 1 (Derivative of an orthogonal matrix) *for every orthogonal matrix* $\mathbf{R}$ *and every parameter* q*, we have*

$$\frac{\partial \mathbf{R}}{\partial q} = \boldsymbol{\Delta}_q \mathbf{R}$$

where $\boldsymbol{\Delta}_q$ *is an antisymmetric* 3×3 *matrix denoted* $\boldsymbol{\Delta}_q = \mathbf{X}(\mathbf{s})$*, and which satisfies*

$$\boldsymbol{\Delta}_q = \frac{\partial \mathbf{R}}{\partial q} \mathbf{R}^T$$

Computation of a partial derivative of $\mathbf{R}$ *can thus always be reduced to the computation of the three components of a vector* $\mathbf{s}$*.*

Proof:
Every rotation matrix $\mathbf{R}$ is orthogonal, which means that

$$\mathbf{R}^T \mathbf{R} = \mathbf{I} \tag{30}$$

Thus, differentiating the equality (30) with respect to any parameter q of $\mathbf{R}$, gives:

$$\frac{\partial \left(\mathbf{R}^T\right)}{\partial q} \mathbf{R} + \mathbf{R}^T \frac{\partial \mathbf{R}}{\partial q} = 0$$

Multiplying on the left by $\mathbf{R}$ and on the right by $\mathbf{R}^T$, and again using the orthogonality of $\mathbf{R}$, we get the equality:

$$\mathbf{R} \frac{\partial \left(\mathbf{R}^T\right)}{\partial q} = -\frac{\partial \mathbf{R}}{\partial q} \mathbf{R}^T \tag{31}$$

The associativity of the matrix product and the orthogonality of $\mathbf{R}$ allow us to write:

$$\frac{\partial \mathbf{R}}{\partial q} = \frac{\partial \mathbf{R}}{\partial q} \left(\mathbf{R}^T \mathbf{R}\right) = \left(\frac{\partial \mathbf{R}}{\partial q} \mathbf{R}^T\right) \mathbf{R}$$

Now, the matrix coefficient of $\mathbf{R}$ in the last term is antisymmetric, since

$$\left(\frac{\partial \mathbf{R}}{\partial q} \mathbf{R}^T\right)^T = \mathbf{R} \left(\frac{\partial \mathbf{R}}{\partial q}\right)^T = \mathbf{R} \frac{\partial \left(\mathbf{R}^T\right)}{\partial q} = -\frac{\partial \mathbf{R}}{\partial q} \mathbf{R}^T$$

where the last equality is due to equation (31). □

B.3 Study of R

B.3.1 Differentiation of R by rotation vector r

The derivatives of θ, f and g are respectively:

$$\frac{\partial\theta}{\partial q} = \frac{\mathbf{r}.\frac{\partial \mathbf{r}}{\partial q}}{\theta} \quad ; \quad \frac{\partial f(\theta)}{\partial q} = (h(\theta) - g(\theta)) \left(\mathbf{r}.\frac{\partial \mathbf{r}}{\partial q}\right) \quad ; \quad \frac{\partial g(\theta)}{\partial q} = (f(\theta) - 2g(\theta))\frac{\mathbf{r}.\frac{\partial \mathbf{r}}{\partial q}}{\theta^2}$$

in which $h(\theta) = \dfrac{1 - f(\theta)}{\theta^2}$.

We calculate:

$$\begin{aligned}
\boldsymbol{\Delta}_p &= \frac{\partial \mathbf{R}}{\partial q}\mathbf{R}^T = \frac{\partial \mathbf{R}}{\partial q}\left(\mathbf{I} - f(\theta)\mathbf{X}(\mathbf{r}) + g(\theta)\mathbf{X}(\mathbf{r})^2\right) \\
&\quad \text{using } \mathbf{X}(\mathbf{r})^3 = -\theta^2\mathbf{X}(\mathbf{r}) \text{ and } \mathbf{X}(\mathbf{r})^4 = -\theta^2\mathbf{X}(\mathbf{r})^2 \\
&= \left[h(\theta) - g(\theta) - \theta^2 g(\theta)h(\theta) + \theta^2 g^2(\theta) + f^2(\theta) - 2f(\theta)g(\theta)\right]\left(\mathbf{r}.\frac{\partial \mathbf{r}}{\partial q}\right)\mathbf{X}(\mathbf{r}) \\
&\quad + \left[f(\theta) - 2g(\theta) - \theta^2 f(\theta)h(\theta) + \theta^2 f(\theta)g(\theta) - \theta^2 f(\theta)g(\theta) + 2\theta^2 g^2(\theta)\right]\frac{\mathbf{r}.\frac{\partial \mathbf{r}}{\partial q}}{\theta^2}\mathbf{X}(\mathbf{r})^2 \\
&\quad + f(\theta)\mathbf{X}(\frac{\partial \mathbf{r}}{\partial q}) + \left[g(\theta) - f^2(\theta) - \theta^2 g^2(\theta)\right]\mathbf{X}(\frac{\partial \mathbf{r}}{\partial q})\mathbf{X}(\mathbf{r}) \\
&\quad + g(\theta)\mathbf{X}(\mathbf{r})\mathbf{X}(\frac{\partial \mathbf{r}}{\partial q}) - f(\theta)g(\theta)\mathbf{X}(\mathbf{r})\mathbf{X}(\frac{\partial \mathbf{r}}{\partial q})\mathbf{X}(\mathbf{r}) + g^2(\theta)\mathbf{X}(\mathbf{r})\mathbf{X}(\frac{\partial \mathbf{r}}{\partial q})\mathbf{X}(\mathbf{r})^2 \\
&= [h(\theta) - f(\theta)g(\theta)]\left(\mathbf{r}.\frac{\partial \mathbf{r}}{\partial q}\right)\mathbf{X}(\mathbf{r}) + g^2(\theta)\left(\mathbf{r}.\frac{\partial \mathbf{r}}{\partial q}\right)\mathbf{X}(\mathbf{r})^2 + f(\theta)\mathbf{X}(\frac{\partial \mathbf{r}}{\partial q}) \\
&\quad - g(\theta)\mathbf{X}(\frac{\partial \mathbf{r}}{\partial q})\mathbf{X}(\mathbf{r}) + g(\theta)\mathbf{X}(\mathbf{r})\mathbf{X}(\frac{\partial \mathbf{r}}{\partial q}) - f(\theta)g(\theta)\mathbf{X}(\mathbf{r})\mathbf{X}(\frac{\partial \mathbf{r}}{\partial q})\mathbf{X}(\mathbf{r}) \\
&\quad + g^2(\theta)\mathbf{X}(\mathbf{r})\mathbf{X}(\frac{\partial \mathbf{r}}{\partial q})\mathbf{X}(\mathbf{r})^2
\end{aligned}$$

These expressions can be simplified using the following observations:

- $\mathbf{X}(\mathbf{u})\mathbf{X}(\mathbf{v}) - \mathbf{X}(\mathbf{v})\mathbf{X}(\mathbf{u}) = \mathbf{X}(\mathbf{u} \wedge \mathbf{v})$
- $\mathbf{X}(\mathbf{u})\mathbf{X}(\mathbf{v})\mathbf{X}(\mathbf{u}) = -(\mathbf{v}.\mathbf{u})\mathbf{X}(\mathbf{u})$
- since $\mathbf{u} \wedge (\mathbf{v} \wedge \mathbf{w}) = (\mathbf{w}.\mathbf{u})\mathbf{v} - (\mathbf{u}.\mathbf{v})\mathbf{w}$ we have

$$\left(\mathbf{r}.\frac{\partial \mathbf{r}}{\partial q}\right)\mathbf{X}(\mathbf{r}) = \theta^2\mathbf{X}(\frac{\partial \mathbf{r}}{\partial q}) + \mathbf{X}\left(\mathbf{r} \wedge \left(\mathbf{r} \wedge \frac{\partial \mathbf{r}}{\partial q}\right)\right)$$

We finally obtain the relation:

$$\begin{aligned}\boldsymbol{\Delta}_p &= \mathbf{X}\left(\frac{\partial \mathbf{r}}{\partial q}\right) + g(\theta)\mathbf{X}\left(\mathbf{r}\wedge\frac{\partial \mathbf{r}}{\partial q}\right) + h(\theta)\mathbf{X}\left(\mathbf{r}\wedge\left(\mathbf{r}\wedge\frac{\partial \mathbf{r}}{\partial q}\right)\right)\\ &= \mathbf{X}\left(\mathbf{H}(\mathbf{r})\frac{\partial \mathbf{r}}{\partial q}\right)\end{aligned}$$

in which

$$\mathbf{H}(\mathbf{r}) = \mathbf{I} + g(\theta)\mathbf{X}(\mathbf{r}) + h(\theta)\mathbf{X}(\mathbf{r})^2 \tag{32}$$

The interested reader may check that this form is equivalent to the one given by Ayache [2]:

$$\boldsymbol{\Delta}_p = \mathbf{X}(\mathbf{s}) \quad \text{with} \quad \mathbf{s} = \left(\mathbf{r}.\frac{\partial \mathbf{r}}{\partial q}\right)\frac{1-f(\theta)}{\theta^2}\mathbf{r} + f(\theta)\frac{\partial \mathbf{r}}{\partial q} + g(\theta)\mathbf{r}\wedge\frac{\partial \mathbf{r}}{\partial q}$$

B.3.2 Singularities and inverse of $\mathbf{H}(\mathbf{r})$

After carrying out the computations, we find:

$$|\mathbf{H}(\mathbf{r})| = 2g(\theta) = 2\frac{1-\cos\theta}{\theta^2}$$

This shows that the matrix $\mathbf{H}(\mathbf{r})$ is defined for $\theta \in]-2\pi, 2\pi[$.

To compute the inverse of $\mathbf{H}(\mathbf{r})$, we solve the general problem of finding the inverse of any matrix $\mathbf{M}$ of the form $\mathbf{I} + a\mathbf{X}(\mathbf{r}) + b\mathbf{X}(\mathbf{r})^2$.

We may look for an inverse matrix of the same form, i.e. $\mathbf{N} = \mathbf{I} + c\mathbf{X}(\mathbf{r}) + d\mathbf{X}(\mathbf{r})^2$, and we have to solve $\mathbf{MN} = \mathbf{I}$.

Recalling that we have $\mathbf{X}(\mathbf{r})^3 = -\theta^2\mathbf{X}(\mathbf{r})$ (so that $\mathbf{X}(\mathbf{r})^4 = -\theta^2\mathbf{X}(\mathbf{r})^2$), $\mathbf{MN} = \mathbf{I}$ is equivalent to:

$$\left\{\begin{array}{lllllll} c(1-\theta^2 b) & + & d(-\theta^2 a) & + & a & = & 0 \\ c(a) & + & d(1-\theta^2 b) & + & b & = & 0 \end{array}\right.$$

which has a single solution if and only if $(1-\theta^2 b)^2 + \theta^2 a^2 \neq 0$. With $a = g(\theta)$ and $b = h(\theta)$, it transpires that the above system has a single solution if and only if $2\frac{1-\cos\theta}{\theta^2} \neq 0$ (i.e. $|\mathbf{H}(\mathbf{r})| \neq 0$, which is not surprising).

In case of $g(\theta) \neq 0$, we can explicitly compute c and d by:

$$\begin{aligned} c &= \frac{1}{2\,g(\theta)}\Big(h(\theta)(-\theta^2 g(\theta)) - g(\theta)(1-\theta^2 h(\theta))\Big) &&= -\frac{1}{2}\\ d &= \frac{1}{2\,g(\theta)}\Big(g(\theta)(g(\theta)) - h(\theta)((1-\theta^2 h(\theta))\Big) &&= \frac{2\,g(\theta) - f(\theta)}{2\,\theta^2\,g(\theta)}\end{aligned}$$

When defined, the inverse of $\mathbf{H}(\mathbf{r})$ is given by:

$$\mathbf{H}(\mathbf{r})^{-1} = \mathbf{I} - \frac{1}{2}\mathbf{X}(\mathbf{r}) + \frac{2g(\theta) - f(\theta)}{2\theta^2 g(\theta)}\mathbf{X}(\mathbf{r})^2 \tag{33}$$

B.3.3 Derivative of $\mathbf{H}(\mathbf{r})$

The derivative of h is:

$$\frac{\partial h(\theta)}{\partial q} = (g(\theta) - 3h(\theta))\frac{\mathbf{r}.\frac{\partial \mathbf{r}}{\partial q}}{\theta^2}$$

Differentiating equation (32), we obtain:

$$\begin{aligned}\frac{\partial \mathbf{H}(\mathbf{r})}{\partial q} &= (f(\theta) - 2g(\theta))\frac{\mathbf{r}.\frac{\partial \mathbf{r}}{\partial q}}{\theta^2}\mathbf{X}(\mathbf{r}) + g(\theta)\mathbf{X}(\frac{\partial \mathbf{r}}{\partial q}) \\ &\quad + (g(\theta) - 3h(\theta))\frac{\mathbf{r}.\frac{\partial \mathbf{r}}{\partial q}}{\theta^2}\mathbf{X}(\mathbf{r})^2 + h(\theta)\left[\mathbf{X}(\mathbf{r})\mathbf{X}(\frac{\partial \mathbf{r}}{\partial q}) + \mathbf{X}(\frac{\partial \mathbf{r}}{\partial q})\mathbf{X}(\mathbf{r})\right]\end{aligned}$$

The temporal derivative of $\mathbf{H}(\mathbf{r})$ is:

$$\begin{aligned}\dot{\mathbf{H}}(\mathbf{r}) &= (f(\theta) - 2g(\theta))\frac{\mathbf{r}.\dot{\mathbf{r}}}{\theta^2}\mathbf{X}(\mathbf{r}) + g(\theta)\mathbf{X}(\dot{\mathbf{r}}) \\ &\quad + (g(\theta) - 3h(\theta))\frac{\mathbf{r}.\dot{\mathbf{r}}}{\theta^2}\mathbf{X}(\mathbf{r})^2 + h(\theta)\left[\mathbf{X}(\mathbf{r})\mathbf{X}(\dot{\mathbf{r}}) + \mathbf{X}(\dot{\mathbf{r}})\mathbf{X}(\mathbf{r})\right]\end{aligned}$$

In many equations, we have to calculate $\dot{\mathbf{H}}(\mathbf{r})\dot{\mathbf{r}}$:

$$\dot{\mathbf{H}}(\mathbf{r})\dot{\mathbf{r}} = (f(\theta) - 2g(\theta))\frac{\mathbf{r}.\dot{\mathbf{r}}}{\theta^2}\mathbf{r} \wedge \dot{\mathbf{r}} + (g(\theta) - 3h(\theta))\frac{\mathbf{r}.\dot{\mathbf{r}}}{\theta^2}\mathbf{r} \wedge (\mathbf{r} \wedge \dot{\mathbf{r}}) + h(\theta)\dot{\mathbf{r}} \wedge (\mathbf{r} \wedge \dot{\mathbf{r}})$$

The following remarks simplify the computation:

- $\mathbf{r} \wedge (\mathbf{r} \wedge \dot{\mathbf{r}}) = \mathbf{r}(\mathbf{r}.\dot{\mathbf{r}}) - \dot{\mathbf{r}}\theta^2$
- $\dot{\mathbf{r}} \wedge (\mathbf{r} \wedge \dot{\mathbf{r}}) = \mathbf{r}\dot{\mathbf{r}}^2 - \dot{\mathbf{r}}(\mathbf{r}.\dot{\mathbf{r}})$

and finally we obtain

$$\begin{aligned}\dot{\mathbf{H}}(\mathbf{r})\dot{\mathbf{r}} &= \left(\dot{\mathbf{r}}^2 h(\theta) + \frac{(\mathbf{r}.\dot{\mathbf{r}})^2}{\theta^2}[g(\theta) - 3h(\theta)]\right)\mathbf{r} \\ &\quad + (\mathbf{r}.\dot{\mathbf{r}})\left[2h(\theta) - g(\theta)\right]\dot{\mathbf{r}} + \frac{\mathbf{r}.\dot{\mathbf{r}}}{\theta^2}[f(\theta) - 2g(\theta)]\,\mathbf{r} \wedge \dot{\mathbf{r}}\end{aligned} \tag{34}$$

B.3.4 Properties of $\mathbf{H}(\mathbf{r})$

Using equalities (29) and (32), we obtain by direct computation:

$$\mathbf{H}(\mathbf{r})^T = \mathbf{H}(\mathbf{r})\,\mathbf{R}^T = \mathbf{R}^T\,\mathbf{H}(\mathbf{r}) \quad (35)$$

$$\mathbf{H}(\mathbf{r}) = \mathbf{H}(\mathbf{r})^T\,\mathbf{R} = \mathbf{R}\,\mathbf{H}(\mathbf{r})^T \quad (36)$$

Notations

$\dot{(\,)}$, $\ddot{(\,)}$	: first and second derivative with respect to time
$\wedge$	: vector (or cross) product
$\boldsymbol{\nabla}$	: gradient operator
S	: moving solid
R	: reference solid
G	: center of mass of the solid S
E_K	: kinetic energy
E_P	: potential energy
L	: Lagrangian
$\boldsymbol{\gamma}(P)$	: acceleration of point P
$\mathbf{v}(P)$	: velocity of point P
$m(S)$	: mass of the solid S
$p(P)$	: value of of the potential field p generated by R at P
κ	: viscosity constant
$\boldsymbol{\omega}$	: angular velocity vector of S
ρ	: density of the solid S
θ	: rotation angle $\theta = \|\mathbf{r}\|$
$\mathbf{f}$	: force acting on S
$\mathbf{m}(Q)$	: torque acting on S at Q
$\mathbf{f}_p$	: potential force acting on S
$\mathbf{m}_p(Q)$	: potential torque acting on S at Q
$\mathbf{f}_v$	: viscosity force acting on S
$\mathbf{m}_v(Q)$	: viscosity torque acting on S at Q
$\boldsymbol{\delta}(Q)$	: dynamic moment of S computed at Q
$\boldsymbol{\sigma}(Q)$	: kinetic moment of S computed at Q
$\mathbf{n}$, $\mathbf{s}$, $\mathbf{u}$, $\mathbf{v}$, $\mathbf{w}$	: vectors
$\mathbf{r}$	: rotation vector
$\mathbf{t}$	: translation vector
$\mathbf{H}(\mathbf{r})$	: matrix which operates in the derivation of the rotation matrix $\mathbf{R}$
	: (see appendix B)
$\mathbf{I}$	: 3×3 identity matrix
$\mathbf{J}(Q)$	: inertia tensor of S computed at Q
$\mathbf{R}$	: 3×3 rotation matrix
$\mathbf{X}(\mathbf{n})$	: 3×3 antisymmetric matrix of the vector product by $\mathbf{n}$

References

[1] N.M. Alpert, J.F. Bradshaw, D. Kennedy, and J.A. Correia. The principal axes transformation - a method for image registration. *The Journal of Nuclear Medicine*, 31(10), October 1990.

[2] N. Ayache. *Artificial vision for mobile robots: stereo vision and multisensory perception.* MIT Press, 1991.

[3] N. Ayache, A. Guéziec, J.P. Thirion, A. Gourdon, and J. Knoplioch. Evaluating 3-D registration of CT-Scan images using crest lines. In *Geometric Methods in Computer Vision*, San Diego, 1993. SPIE.

[4] R. Bajcsy and S. Kovačič. Multiresolution elastic matching. *Computer Vision, Graphics, and Image Processing*, 46:1–21, 1989.

[5] S. Benayoun, O. Monga, A. Guéziec, and N. Ayache. Using surface curvatures for 3-D image registration. In *Proceedings of the 11th Conference on Computer Application in Radiology (S'CAR 92)*, Baltimore, Maryland, USA, June 1992.

[6] P.J. Besl and N.D. McKay. A method for registration of 3-D shapes. *IEEE Transactions on Pattern Analysis and Machine Intelligence*, 14:239–256, February 1992.

[7] G. Borgefors. Distance transformations in digital images. *Computer Vision, Graphics, and Image Processing*, 34:344–371, 1986.

[8] G. Borgefors. Hierarchical chamfer matching: A parametric edge matching algorithm. *IEEE Transactions on Pattern Analysis and Machine Intelligence*, 10(6):849–865, november 1988.

[9] L.G. Brown. A survey of image registration techniques. *ACM Computing Surveys*, 24(4):325–376, december 1992.

[10] M.E. Brummer, R.M. Mersereau, R.L. Eisner, and R.R.J. Lewine. Automatic detection of brain contours in MRI data sets. *IEEE Transactions on Medical Imaging*, 12(2):153–166, june 1993.

[11] I. Cohen, L.D. Cohen, and N. Ayache. Using deformable surfaces to segment 3-D images and infer differential structures. *Computer Vision, Graphics, and Image Processing: Image Understanding*, 56(2):242–263, September 1992.

[12] A. Collignon, D. Vandermeulen, P. Suetens, and G. Marchal. Registration of 3D multi-modality medical images using surfaces and point landmarks. *Pattern Recognition Letters*, 15:461–467, May 1994.

[13] A. Collignon, D. Vandermeulen, P. Suetens, G. Marchal, A. Baert, and A. Oosterlinck. Automatic registration of 3D images of the brain based on fuzzy objects. In *Medical Imaging 1994: Image Processing*, volume 2167 of *SPIE proceedings series*, Newport Beach, California, USA, February 13-18 1994. SPIE.

[14] D.L. Collins, T.M. Peters, and A.C. Evans. Multiresolution image registration and brain structure segmentation. In *EMBS satellite symposium on 3-D advanced image processing in medicine*, Rennes, France, November 2–4 1992. IEEE.

[15] P.E. Danielsson. Euclidean distance mapping. *Computer Graphics and Image Processing*, 14:227–248, 1980.

[16] R. Declerck, J. Cornelis, and M. Bister. Segmentation of medical images. *Image and Vision Computing*, 11(8):486–503, october 1993.

[17] A.C. Evans, C. Beil, S. Marret, C.J. Thompson, and A. Hakim. Anatomical-functional correlation using an adjustable MRI-based region of interest atlas with positron emission tomography. *Journal of Cerebral Blood Flow Metabolism*, 8:513–529, 1988.

[18] A.C. Evans, P. Neelin, S. Marrett, E. Meyer, W. Dai, and L. Collins. Combined stereotactic mapping of MRI and PET studies of cognitive activation in human brain. In *Proceedings of the 13th Annual International Conference of the IEEE Engineering in Medicine and Biology Society*, volume 13, pages 224–226, Orlando, Florida, USA, October 31 - November 3 1991. Part 1/5.

[19] T.L. Faber, R.W. McColl, R.M. Opperman, J.R. Corbett, and R.M. Peshock. Spatial and temporal registration of cardiac SPECT and MR images: methods and evaluation. *Radiology*, 179(3):857–861, June 1991.

[20] O.D. Faugeras and M. Herbert. The representation, recognition, and locating of 3-D objects. *The International Journal of Robotics Research*, 5(3):27–49, 1986.

[21] J. Feldmar and N. Ayache. Locally affine registration of free-form surfaces. In *Computer Vision and Pattern Recognition (CVPR'94)*, pages 496–501, Seattle, USA, June 1994. IEEE.

[22] S. Fernàndez-Vidal. Mise en correspondance d'images médicales 3D. Master's thesis, Université de Nice-Sophia Antipolis, september 1993. (in french).

[23] W.R. Fright and A.D. Linney. Registration of 3-D head surfaces using multiple landmarks. *IEEE Transactions on Medical Imaging*, 12(3):515–520, september 1993.

[24] G. Gerig and al. Automating segmentation of dual-echo MR head data. In A.C.F. Colchester and D.J. Hawkes, editors, *XIIth international conference on Information Processing in Medical Imaging (IPMI)*, pages 175–187, Wye, Kent, England, July 1991. Lecture notes in Computer Science 511, Heidelberg, Springer Verlag.

[25] C.A. Glasbey. An analysis of histogram-based thresholding algorithms. *Computer Vision, Graphics, and Image Processing: Graphical Models and Image Processing*, 55(6):532–537, november 1993.

[26] D.B. Goldgof, H. Lee, and S. Huang. Matching and motion estimation of three-dimensional point and line sets using eigenstructure without correspondences. *Pattern Recognition*, 25(3):271–286, 1992.

[27] W.E.L. Grimson. *Object recognition by computer: the role of geometric constraints.* MIT Press, 1990.

[28] W.E.L. Grimson, T. Lozano-Pérez, W.M. Wells, G.J. Ettinger, S.J. White, and R. Kikinis. An automatic registration method for frameless stereotaxy, image guided surgery, and enhanced reality visualization. In *Computer Vision and Pattern Recognition (CVPR'94)*, pages 430–436, Seattle, USA, June 1994. IEEE.

[29] A. Guéziec and N. Ayache. Smoothing and matching of 3-D space curves. In *2nd European Conference on Computer Vision (ECCV'92)*, pages 620–629, Santa Margherita, Ligure, Italy, May 18–23 1992.

[30] K.H. Höhne and W. Hanson. Interactive 3-D segmentation of MRI and CT volumes using morphological operations. *Journal of Computer Assisted Tomography*, 16(2):285–294, March/April 1992.

[31] D.L.G. Hill and al. Registration of MR and CT images for skull base surgery using point-like anatomical features. *The British Journal of Radiology*, 64(767):1030–1035, November 1991.

[32] C.K. Hoh and al. Automated iterative three-dimensional registration of positron emission tomography images. *The Journal of Nuclear Medicine*, 34(11):2009–2018, November 1993.

[33] H. Jiang, R. Robb, and K. Holton. A new approach to 3-D registration of multimodality medical images by surface matching. In *Visualization in Biomedical Computing*, volume 1808 of *SPIE proceedings series*, pages 196–213. SPIE, 1992.

[34] M. Joliot and B.M. Mazoyer. Three-dimensional segmentation and interpolation of magnetic resonance brain images. *IEEE Transactions on Medical Imaging*, 12(2):269–277, june 1993.

[35] O. Kübler and G. Gerig. Segmentation and analysis of multidimensional datasets in medicine. In *3-D Imaging in Medicine*, pages 63–81. Springer Verlag, 1990.

[36] S. Lavallée, L. Brunie, B. Mazier, and P. Cinquin. Matching of medical images for computed and robot assisted surgery. In *Proceedings of the 13th Annual International Conference of the IEEE Engineering in Medicine and Biology Society*, volume 13, pages 39–40, Orlando, Florida, USA, October 31 - November 3 1991. Part 1/5.

[37] S. Lavallée, R. Szeliski, and L. Brunie. Matching 3-D smooth surfaces with their 2-D projections using 3-D distance maps. In *Geometric Methods in Computer Vision*. SPIE, July 25–26 1991. San Diego.

[38] M.N. Maisey, D.J. Hawkes, and A.M. Lukawiecki-Vydelingum. Synergistic imaging. *European Journal of Nuclear Medicine*, 19:1002–1005, 1992.

[39] G. Malandain. *Filtrage, topologie et mise en correspondance d'images médicales multidimensionnelles*. PhD thesis, Ecole Centrale de Paris, Septembre 1992.

[40] G. Malandain, G. Bertrand, and N. Ayache. Topological segmentation of discrete surfaces. *International Journal of Computer Vision*, 10(2):183–197, 1993.

[41] G. Malandain, S. Fernández-Vidal, and J.M. Rocchisani. Improving registration of 3-D medical images using a mechanical based method. In *3rd European Conference on Computer Vision (ECCV'94)*, pages 131–136, Stockholm, Sweden, May 2–6 1994. Lecture Notes in Computer Science 801.

[42] G. Malandain and J.M. Rocchisani. Registration of 3-D medical images using a mechanical based method. In *EMBS satellite symposium on 3-D advanced image processing in medicine*, Rennes, France, November 2–4 1992. IEEE.

[43] G. Malandain and J.M. Rocchisani. Matching of 3-D medical images with a potential based method. Technical Report 1890, INRIA, 2004 route des Lucioles BP 93, 06902 Sophia Antipolis Cedex, France, March 1993.

[44] J.F. Mangin, V. Frouin, and B. Bendriem. Nonsupervised 3-D registration of PET and MRI data using chamfer matching. In *Conference on medical imaging, Nuclear Science Symposium*, Orlando, Florida, october 27–31 1992.

[45] C.C. Meltzer and al. Anatomical localization for PET using MR imaging. *Journal of Computer Assisted Tomography*, 14(3):418–426, 1990.

[46] S. Minoshima, K.L. Berger, K.S. Lee, and M.A. Mintun. An automated method for rotational correction and centering of the three-dimensional functional brain images. *The Journal of Nuclear Medicine*, 33:1579–1585, 1992.

[47] O. Monga, S. Benayoun, and O. Faugeras. From partial derivatives of 3-D density images to ridges lines. In *Computer Vision and Pattern Recognition*, pages 354–389, Champaign, Illinois, USA, June 15–18 1992. IEEE.

[48] O. Monga, R. Deriche, G. Malandain, and J.P. Cocquerez. 3-D edge detection by recursive filtering and edge tracking. In *10th International Conference on Pattern Recognition*, Atlantic City, USA, June 17–21 1990.

[49] J.M. Mountz and al. Validation of a reference method for correlation of anatomic and functional brain images. *Computerized Medical Imaging and Graphics*, 18(3):163–174, 1994.

[50] M.A. Oghabian and A. Todd-Pokropek. Registration of brain images by a multi-resolution sequential method. In A.C.F. Colchester and D.J. Hawkes, editors, *XIIth international conference on Information Processing in Medical Imaging (IPMI)*, pages 165–174, Wye, Kent, England, July 1991. Lecture notes in Computer Science 511, Heidelberg, Springer Verlag.

[51] C.A. Pelizzari and al. Accurate three-dimensional registration of CT, PET and/or MR images of the brain. *Journal of Computer Assisted Tomography*, 13(1):20–26, 1989.

[52] C.A. Pelizzari, A.C. Evans, P. Neelin, C.T. Chen, and S. Marrett. Comparison of two methods for 3D registration of PET and MRI images. In *Proceedings of the 13th Annual International Conference of the IEEE Engineering in Medicine and Biology Society*, volume 13, pages 221–223, Orlando, Florida, USA, October 31 - November 3 1991. Part 1/5.

[53] X. Pennec. Correctness and robustness of 3D rigid matching with bounded sensor error. Technical Report 2111, INRIA, 2004 route des Lucioles BP 93, 06902 Sophia Antipolis Cedex, France, November 1993.

[54] F. Preparata and M. Shamos. *Computational Geometry, an Introduction*. Springer Verlag, 1986.

[55] W.H. Press, B.P. Flannery, S.A. Teukolsky, and W.T. Vetterling. *Numerical Recipes in C*. Cambridge University Press, 1988.

[56] S.P. Raya. Low-level segmentation of 3-D magnetic resonance brain images - a rule based system. *IEEE Transactions on Medical Imaging*, 12(3):327–337, 1990.

[57] G. Rizzo, P. Pasquali, M.C. Gilardi, S. Cerutti, and al. Multimodality biomedical image integration: Use of a cross-correlation technique. In *Proceedings of the 13th Annual International Conference of the IEEE Engineering in Medicine and Biology Society*, volume 13, pages 219–220, Orlando, Florida, USA, October 31 - November 3 1991. Part 1/5.

[58] N. Rougon. *Éléments pour la reconnaissance de formes tridimensionnelles déformables - Application à l'imagerie biomédicale*. PhD thesis, École Nationale Supérieure des Télécommunications, Février 1993.

[59] H. Rusinek and al. Principal axes and surface fitting methods for three-dimensional image registration. *The Journal of Nuclear Medicine*, 34(11):2019–2024, November 1993.

[60] J.T. Schwartz and M. Sharir. Identification of partially obscured objects in two and three dimensions by matching noisy characteristic curves. *The International Journal of Robotics Research*, 6(2):29–44, 1987.

[61] J. Serra. *Image analysis and mathematical morphology*, volume 1. Academic Press, 1982.

[62] J. Serra. *Image analysis and mathematical morphology: theoretical advances*, volume 2. Academic Press, 1988.

[63] P. Suetens, P. Fua, and A.J. Hanson. Computational strategies for object recognition. *ACM Computing Surveys*, 24(1):5–61, march 1992.

[64] R. Szeliski and S. Lavallée. Matching 3-D anatomical surfaces with non-rigid deformations using octree-splines. In *Geometric Methods in Computer Vision II*, volume 2031, pages 306–315, San Diego, 1993. SPIE.

[65] J-P. Thirion and S. Benayoun. Image surface extremal points, new features points for image registration. Technical Report 2003, INRIA, 2004 route des Lucioles BP 93, 06902 Sophia Antipolis Cedex, France, August 1993.

[66] J-P Thirion, O. Monga, S. Benayoun, A. Guéziec, and N. Ayache. Automatic registration of 3-D images using surface curvature. In *IEEE Int. Symp. on Optical Applied Science and Engineering*, San-Diego, July 1992.

[67] T.G. Turkington and al. Accuracy of registration of PET, SPECT and MR images of a brain phantom. *The Journal of Nuclear Medicine*, 34(9):1587–1594, September 1993.

[68] P.A. van den Elsen. *Multimodality Matching of Brain Images.* PhD thesis, Utrecht University, 1993. ISBN number: 90-71546-02-0.

[69] P.A. van den Elsen, J.B. Antoine Maintz, E.J.D. Pol, and M.A. Viergever. Image fusion using geometrical features. In *Visualization in Biomedical Computing*, volume 1808 of *SPIE proceedings series*, pages 172–186. SPIE, 1992.

[70] P.A. van den Elsen, E.J.D. Pol, and M.A. Viergever. Medical image matching - a review with classification. *IEEE Engineering in Medicine and Biology*, 12(4):26–39, march 1993.

[71] A. Venot, J.F. Lebruchec, and J.C. Roucayrol. A new class of similarity measures for robust image registration. *Computer Vision, Graphics, and Image Processing*, 28:176–184, 1984.

[72] R.P. Woods, S.R. Cherry, and J.C. Mazziotta. Rapid automated algorithm for aligning and resclicing PET images. *Journal of Computer Assisted Tomography*, 16(1):1–14, 1992.

[73] J. Zhang and al. Multimodality imaging of brain structures for stereotactic surgery. *Radiology*, 175(2):435–441, May 1990.

[74] Z. Zhang. Iterative point matching for registration of free-form curves and surfaces. *International Journal of Computer Vision*, 13(2):119–152, 1994.

[75] A.P. Zijdenbos, B.M. Dawant, and R.A. Margolin. Automatic detection of intracranial contours in MR images. *Computerized Medical Imaging and Graphics*, 18(1):11–23, January-February 1994.

[76] G. Zubal, H. Tagare, L. Zhang, and J. Duncan. 3-D registration of intermodality medical images. In *Proceedings of the 13th Annual International Conference of the IEEE Engineering in Medicine and Biology Society*, volume 13, pages 293–294, Orlando, Florida, USA, October 31 - November 3 1991. Part 1/5.

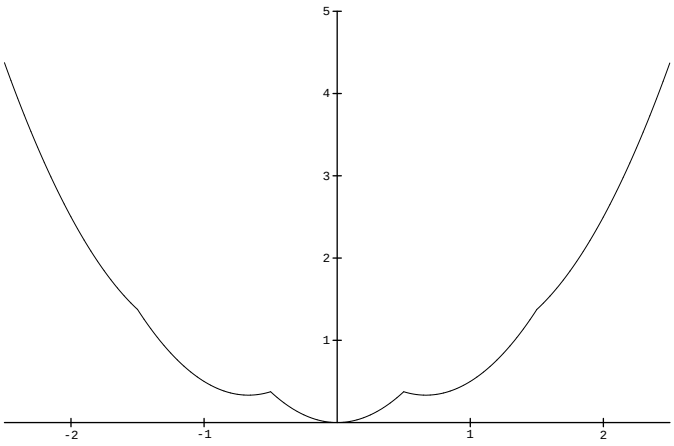

Figure 6: Potential energy of $S(x)$ in the potential field generated by M with $d = 1.0$.

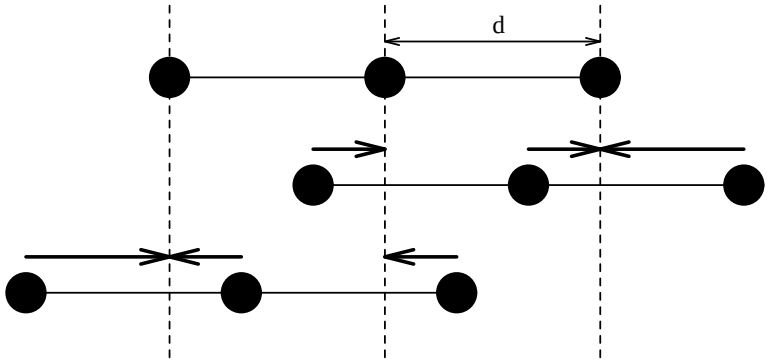

Figure 7: The two local minima: the sum of forces which apply to the three points is equal to $\vec{0}$.

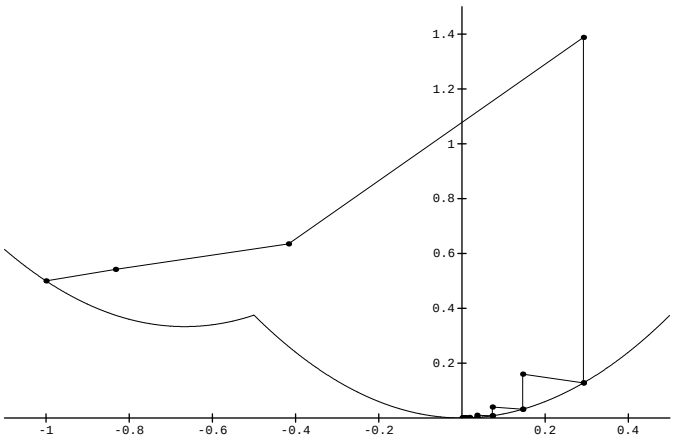

Figure 8: Behavior of our method (with only the heuristic of figure 2) with a start position $x = -d$, dots represent the successive positions of $S(x)$, lines between them represent the whole solid energy (sum of potential and kinetic energies), with $dt = 1$. We find the global minimum.

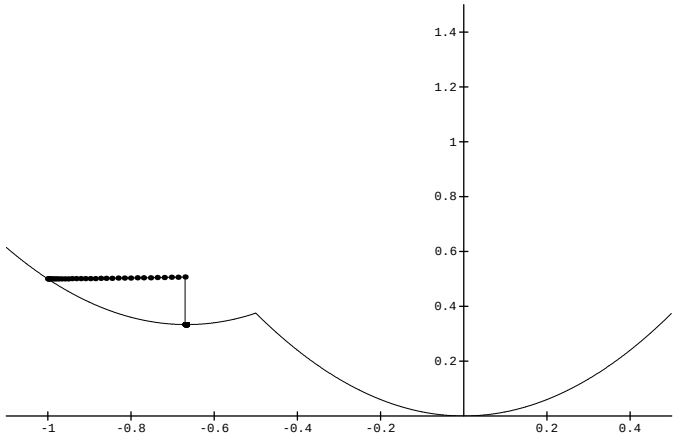

Figure 9: Behavior of our method (with only the heuristic of figure 2) with a start position $x = -d$, dots represent the successive positions of $S(x)$, lines between them represent the whole solid energy, with $dt = 0.05$. We are trapped by the local minimum.

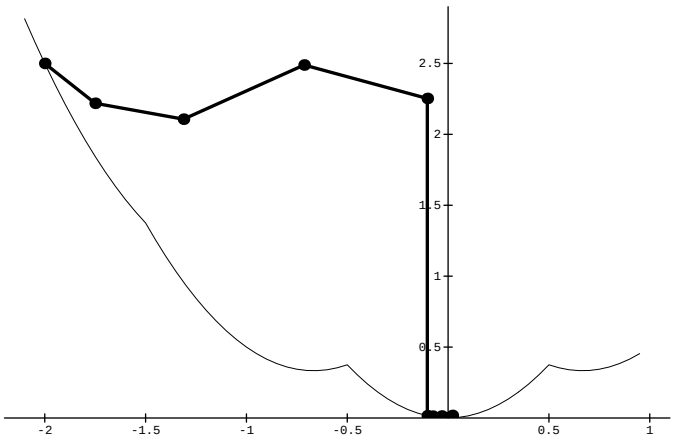

Figure 10: Behavior of our method with a start position $x = -2d$, dots represent the successive positions of $S(x)$, lines between them represent the whole solid energy (sum of potential and kinetic energies), with $dt = 0.5$. We use Euler methods as update rules and the heuristic of figure 2 to minimize the energy.

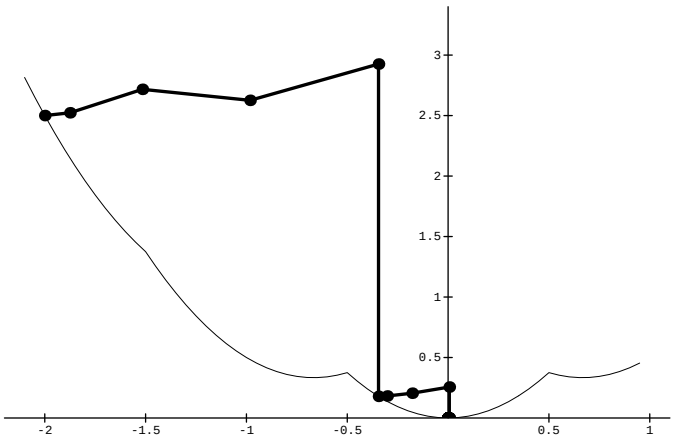

Figure 11: Behavior of our method with a start position $x = -2d$, dots represent the successive positions of $S(x)$, lines between them represent the whole solid energy (sum of potential and kinetic energies), with $dt = 0.5$. We use Taylor expansions as update rules and the heuristic of figure 2 to minimize the energy.

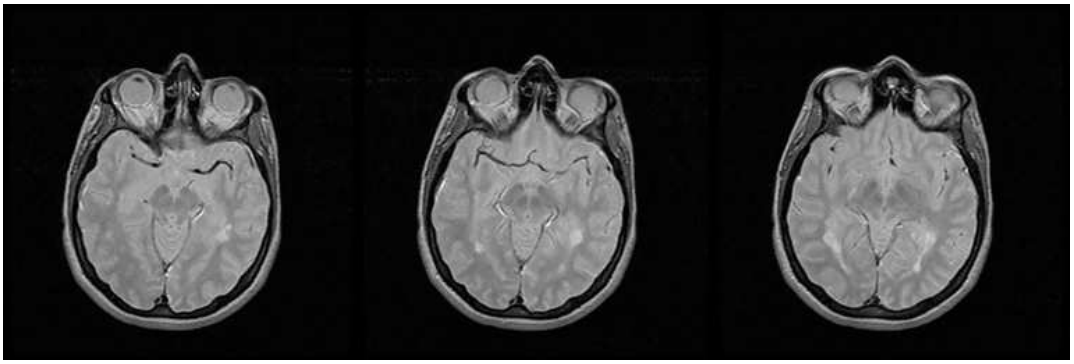

Figure 12: Three consecutive slices of a MRI image of a brain. Please notice the horizontal thin black structure (the middle cerebral artery) at the top of the brain in the central slice. Data are provided by Ron Kikinis, M.D., Department of Radiology, Brigham and Women's Hospital, Harvard Medical School, Boston, MA.

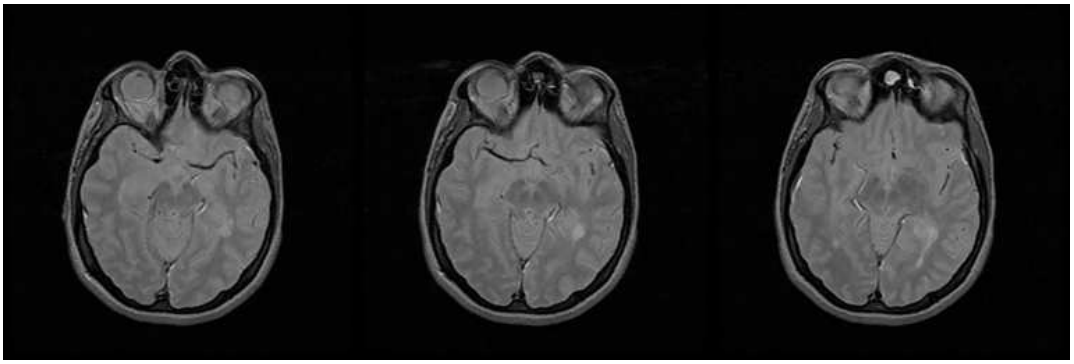

Figure 13: Three consecutive slices of a second MRI study of the same brain two months later. We try to show the same slices as in figure 12. Please notice that the middle cerebral artery does not appear completely at the top of the brain in the central slice. Data are provided by Ron Kikinis, M.D., Department of Radiology, Brigham and Women's Hospital, Harvard Medical School, Boston, MA.

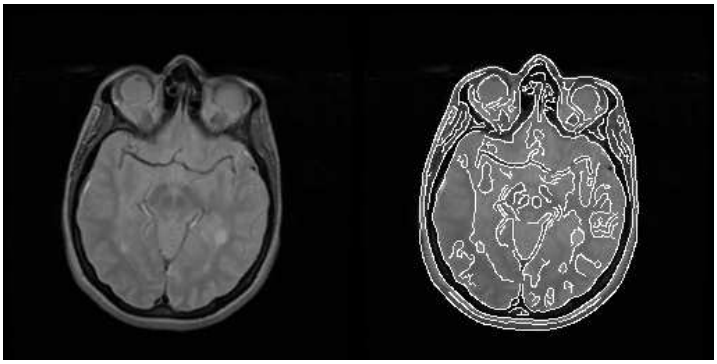

Figure 14: From left to right: after registration, the slice of the second resampled data volume corresponding to the central slice of figure 12: please notice that the middle cerebral artery now appears completely; edges extracted from the central slice of figure 12 superimposed on the slice shown on the left.

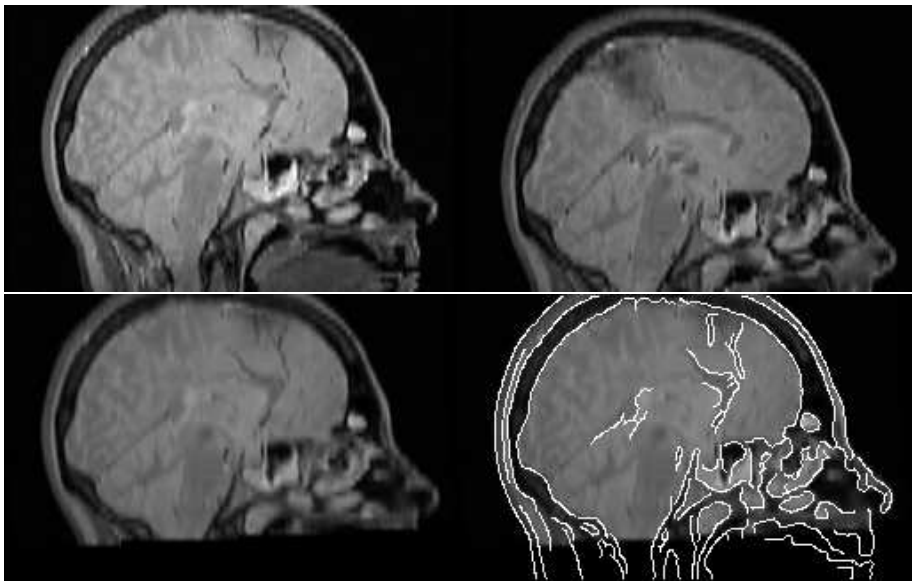

Figure 15: From top to bottom and from left to right: a sagittal slice of the first original scan image, a sagittal slice of the second original scan image, the slice of the second resampled data volume corresponding to the sagittal slice of the first scan (after registration), and edges extracted from the sagittal slice of the first scan superimposed on the resampled slice. Images seem blurred because of the second resampling we made along the vertical axis in order to obtain quasi-isotropic voxels (for display purpose only).

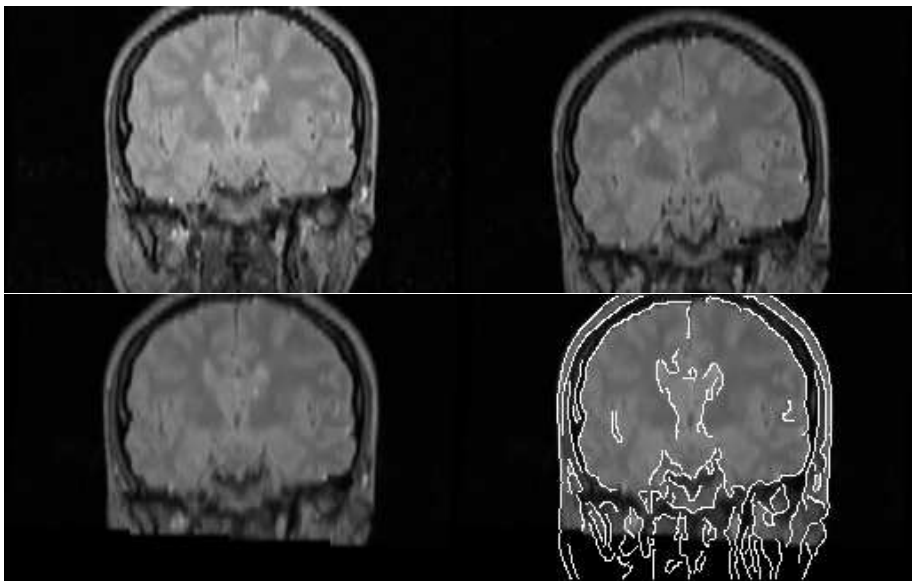

Figure 16: Same as figure 15 with coronal slices.

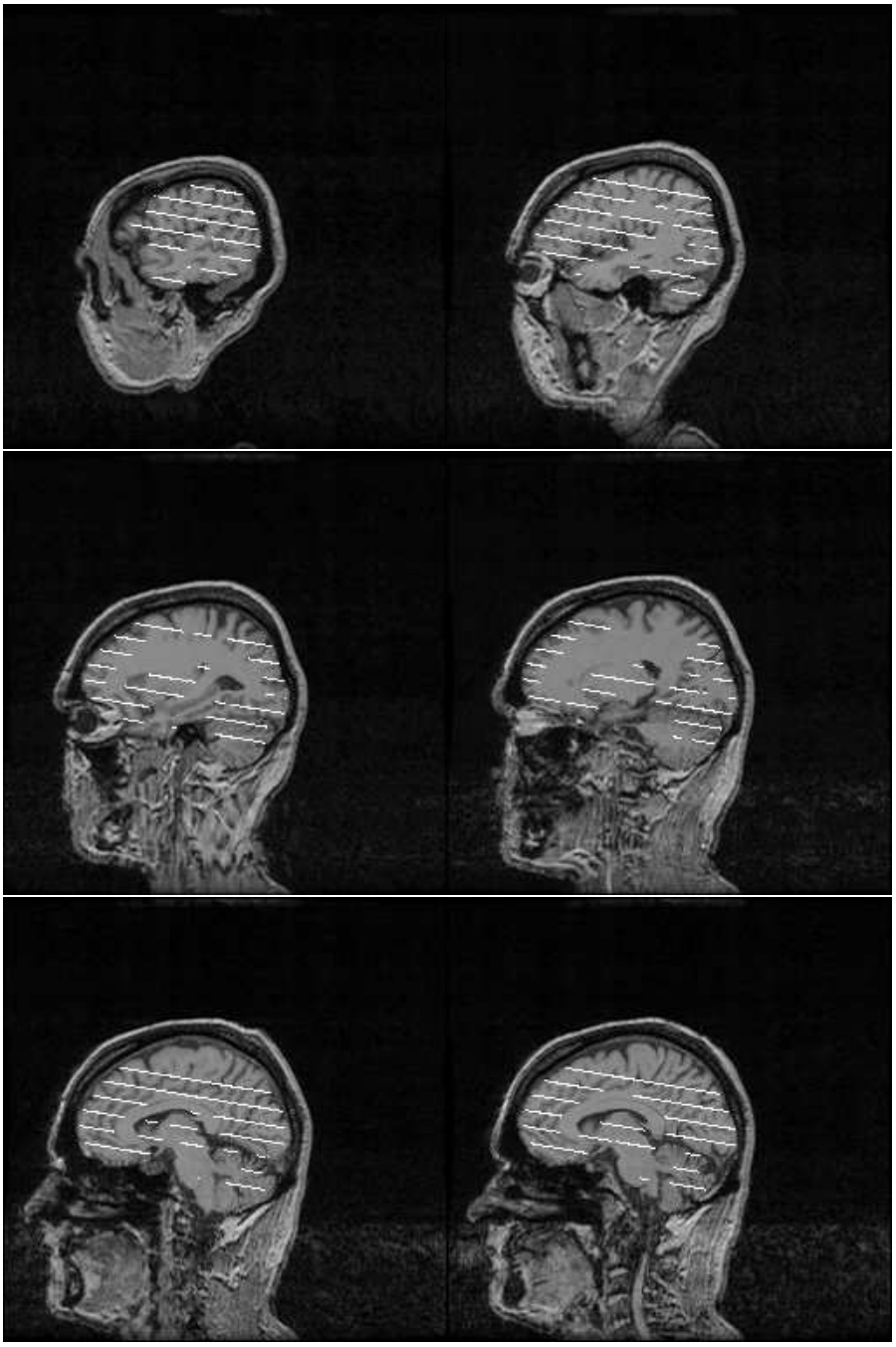

Figure 17: After registration, the trace of the seven PET slices on the MRI slices. Images are courtesy of Dr. Jael Travere of Cyceron center (CEA, Caen, France).

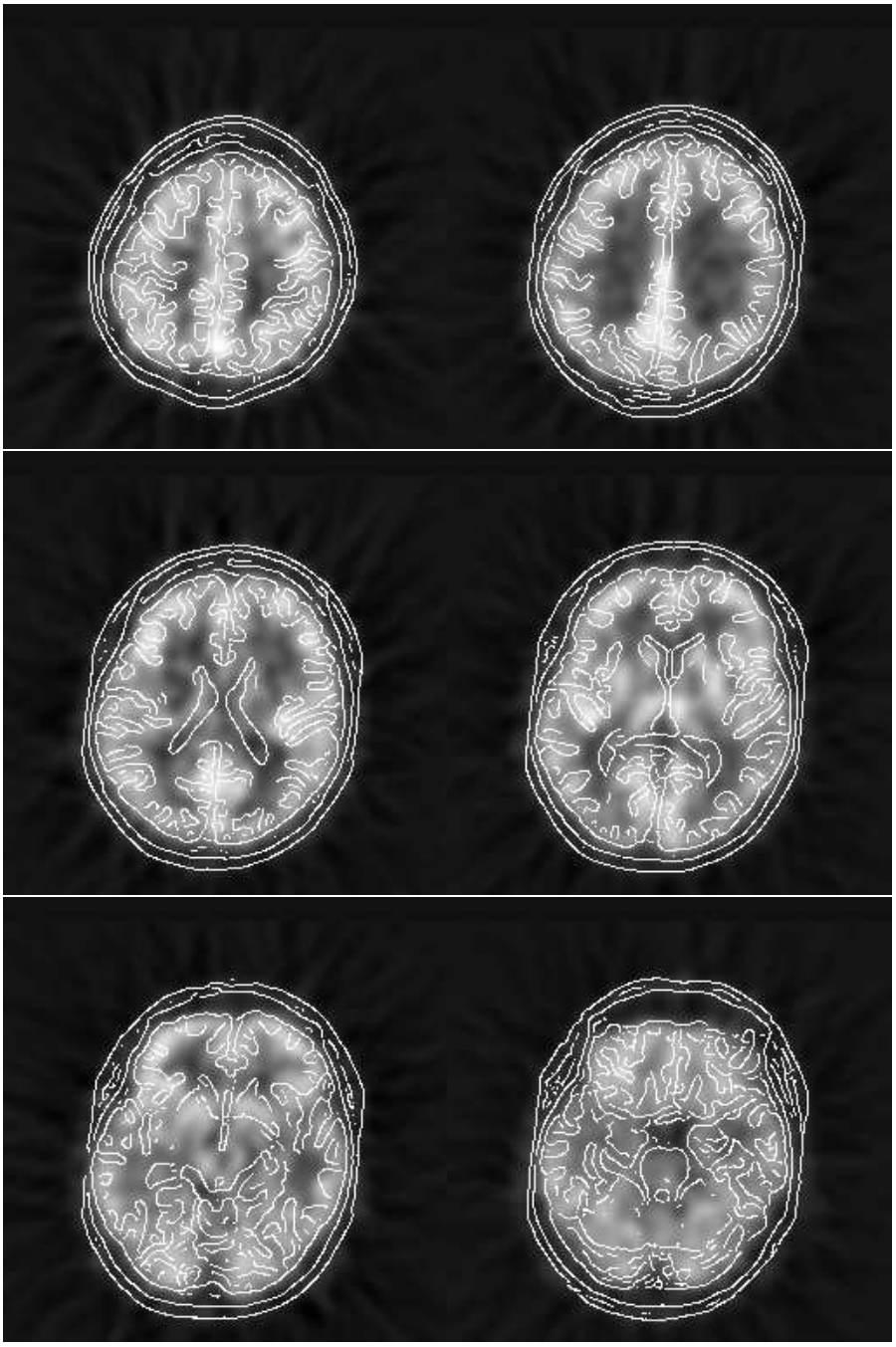

Figure 18: Anatomical edges (computed from MRI image) corresponding to the PET slices.

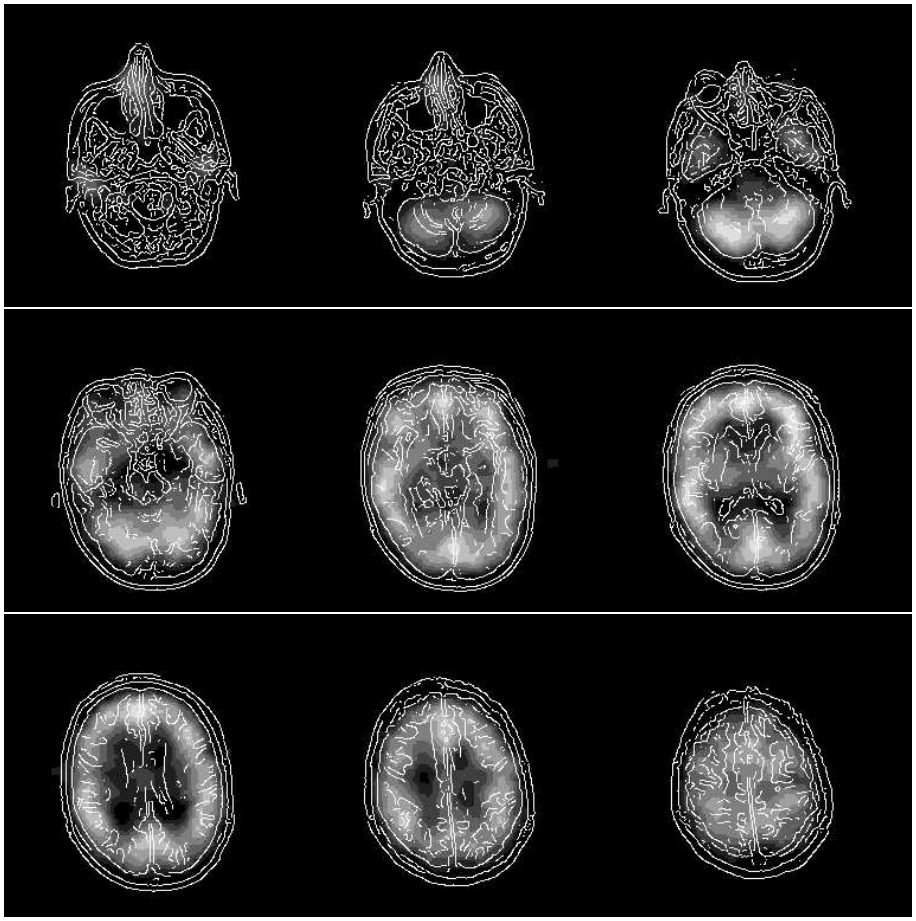

Figure 19: Anatomical edges (computed from MRI image) corresponding to the resampled SPECT slices. Images are courtesy of Philippe Boulle (Focus Medical, Grenoble, France).

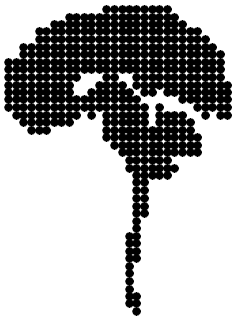

Figure 20: Initial binary image of 64 × 64 pixels: the object is made of 463 points.

Figure 21: Subsampling of the binary image of figure 20. From left to right, we collect a block of respectively 2x2x2, 4x4x4 and 8x8x8 pixels, and the number of points are respectively 144, 49, and 16 in the resampled lists. Each point is represented by a disk, whose size is proportional to its associated volume.

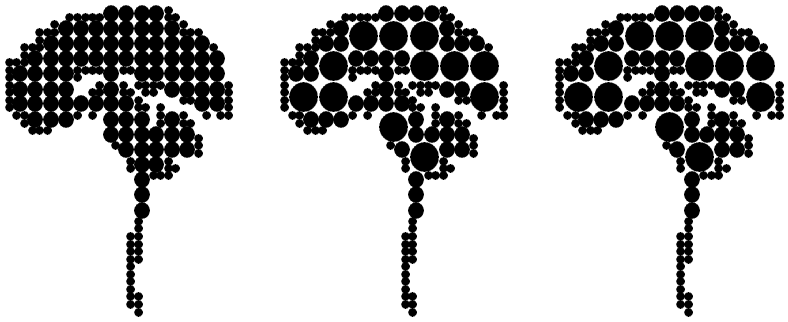

Figure 22: Quadtree-like subsampling of the binary image of figure 20. From left to right, the initial examinated block was respectively of 2x2x2, 4x4x4 and 8x8x8 pixels, and the number of points are respectively 196, 160, and 160 in the resampled lists.

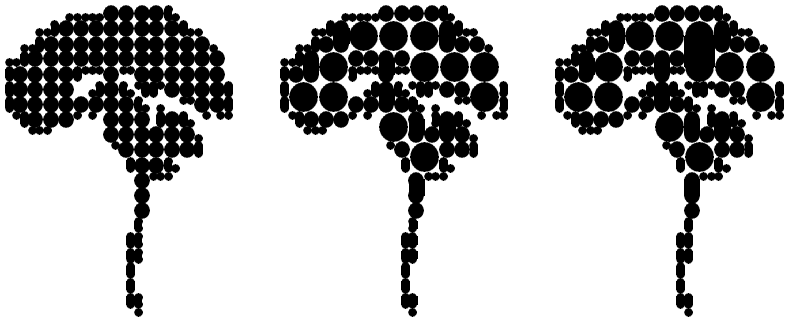

Figure 23: Kdtree-like subsampling of the binary image of figure 20. From left to right, the initial examinated block was respectively of 2x2x2, 4x4x4 and 8x8x8 pixels, and the number of points are respectively 165, 121, and 120 in the resampled lists.

Unité de recherche INRIA Lorraine, Technopôle de Nancy-Brabois, Campus scientifique,
615 rue du Jardin Botanique, BP 101, 54600 VILLERS LÈS NANCY
Unité de recherche INRIA Rennes, Irisa, Campus universitaire de Beaulieu, 35042 RENNES Cedex
Unité de recherche INRIA Rhône-Alpes, 46 avenue Félix Viallet, 38031 GRENOBLE Cedex 1
Unité de recherche INRIA Rocquencourt, Domaine de Voluceau, Rocquencourt, BP 105, 78153 LE CHESNAY Cedex
Unité de recherche INRIA Sophia-Antipolis, 2004 route des Lucioles, BP 93, 06902 SOPHIA-ANTIPOLIS Cedex

Éditeur
INRIA, Domaine de Voluceau, Rocquencourt, BP 105, 78153 LE CHESNAY Cedex (France)
ISSN 0249-6399